RADIATION RESPONSE OF STRAINED SILICON-GERMANIUM SUPERLATTICES

A Thesis

by

MICHAEL SCOTT MARTIN

Submitted to the Office of Graduate Studies of
Texas A&M University
in partial fulfillment of the requirements for the degree of

MASTER OF SCIENCE

May 2010

Major Subject: Nuclear Engineering

RADIATION RESPONSE OF STRAINED SILICON-GERMANIUM SUPERLATTICES

A Thesis

by

MICHAEL SCOTT MARTIN

Submitted to the Office of Graduate Studies of
Texas A&M University
in partial fulfillment of the requirements for the degree of

MASTER OF SCIENCE

Approved by:

Chair of Committee,	Lin Shao
Committee Members,	Sean McDeavitt
	Xinghang Zhang
Head of Department,	Raymond Juzaitis

May 2010

Major Subject: Nuclear Engineering

ABSTRACT

Radiation Response of Strained Silicon-Germanium Superlattices. (May 2010)

Michael Scott Martin, B.S., Texas A&M University

Chair of Advisory Committee: Dr. Lin Shao

The purpose of this study is to investigate the role of strain in the accumulation of crystalline defects created by ion irradiation. Previous studies state that strained $Si_{1-x}Ge_x$ is more easily amorphized by ion irradiation than unstrained, bulk Si in a periodic superlattice structure; however, the reason for preferential amorphization of the strained $Si_{1-x}Ge_x$ layer in the periodic structure of strained and unstrained layers is not well understood.

In this study, various ion irradiations will be carried out on SiGe strained layer superlattices grown on (100)-orientation bulk Si by low temperature molecular beam epitaxy. The samples under investigation are 50 nm surface $Si_{0.8}Ge_{0.2}$/bulk Si and 50 nm surface Si/60 nm $Si_{0.8}Ge_{0.2}$/bulk Si.

Defects will be created in both surface and buried SiGe strained layers by medium and high energy light ion irradiation. The amount of permanently displaced atoms will be quantified by channeling Rutherford backscattering spectrometry. The amorphization model, the path to permanent damage creation, of bulk Si and surface strained SiGe will be investigated. The strain in surface and buried $Si_{0.8}Ge_{0.2}$ layers will be measured by comparison to bulk Si with Rutherford backscattering spectrometry by a novel technique, channeling analysis by multi-axial Rutherford backscattering spectrometry, and the limitations of measuring strain by this technique will be explored.

Results of this study indicated that the amorphization model, the number of ion collision cascades that must overlap to cause permanent damage, of strained

$Si_{0.8}Ge_{0.2}$ is similar to that of bulk Si, suggesting that point defect recombination is less efficient in strained $Si_{0.8}Ge_{0.2}$. Additionaly, a surface strained $Si_{0.8}Ge_{0.2}$ is less stable under ion irradiation than buried strained $Si_{0.8}Ge_{0.2}$. Repeated analysis by multi-axial channeling Rutherford backscattering spectrometry, which requires high fluence of 2 MeV He ions, proved destructive to the surface strained $Si_{0.8}Ge_{0.2}$ layer.

To Sherrie, Dennis and Eric, and to Kim

ACKNOWLEDGMENTS

Thanks to Avery Bingham, Celestino Abrego, Dr. Jesse Carter and Dr. Ron Hart, who taught me a great deal about what it takes to carry out experimental research when I was an undergraduate student, especially Jesse and Dr. Hart. Thanks to Dr. Lin Shao and Mark Hollander for teaching me how to be a competent and productive experimental researcher and technician. Thanks to Assel Aitkalieva, Wei Hua, Kathryn Mews and Aaron Totemeier for being patient as Jesse and I attempted to teach you all how to operate the 150 kV accelerator, during which I learned more about its operation than you "students" did. And many, many thanks to my fellow graduate students, Assel, Di Chen and Michael Myers, as well as McIan Amos, Michael General and Josey Wallace, for your positive attitude and willingness to help each other and me navigate the constant challenges of being part of a productive research group.

TABLE OF CONTENTS

CHAPTER Page

LIST OF TABLES

LIST OF FIGURES

FIGURE Page

FIGURE Page

FIGURE Page

FIGURE Page

CHAPTER I

INTRODUCTION TO ION ACCELERATORS

Two ion accelerators were used in this study: a 150 kV terminal voltage linear ion accelerator at Texas A&M University and a 1.7 MV tandem accelerator at the Texas Center for Superconductivity at the University of Houston. The process of extracting the He ion beam in both accelerators is similar. Figure 1 shows the components in the 150 kV ion accelerator at Texas A&M University.

He ions are created by feeding He gas into the Physicon ion source through bleed valves. The pressure in the ion source is around 3×10^{-6} torr. The ion source contains a W cathode filament heated to eject electrons and an anode biased at around 100 V to impart energy to the ejected electrons in order to ionize the He gas. A Cu wire electromagnet encircles the source to control the size of the plasma created by ionization of He gas. Two negatively biased electrodes pull the ionized gas out of the source through the source aperture. The acceleration column, which consists of many conical electrodes, imparts high voltage to the ion beam. In the glass cross, before the beam is seperated by mass, the total current of all ionized gas can be measured. Also, there is a set of vertical deflection plates to optimize beam steering into the seperator magnet. Mass seperation is done by the seperator magnet with maximum field of 0.7 T through a deflection in the beam line of 15°.

After the seperator magnet, the pressure in the beamline is around 6×10^{-7} torr and the beam can be swept across an area in order to uniformly implant a sample with He ions. For implantations, the beam is deflected off the target by the seperator magnet and steered onto the target by the sweeping magnet. This is done to deflect

---

The journal model is *IEEE Transactions on Automatic Control.*

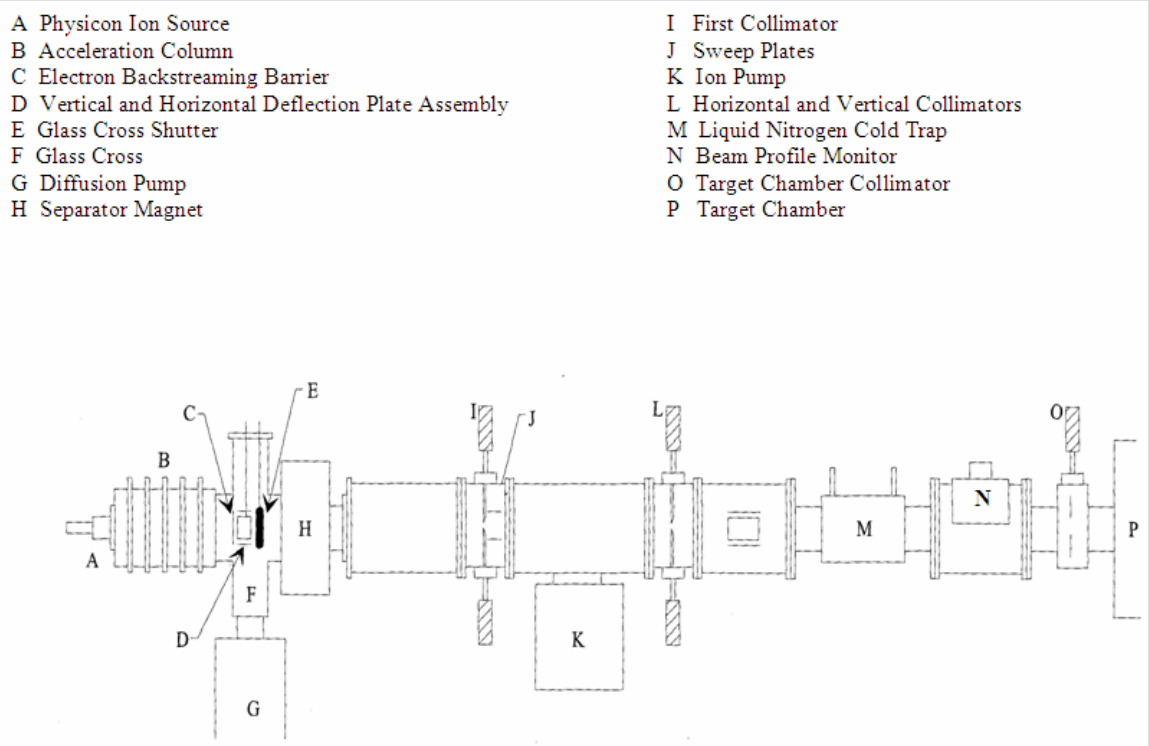

Fig. 1. Schematic of the components in the 150 kV ion accelerator at Texas A&M University.

any neutral particles created by interactions within the beam or between the beam and residual gas atoms. Residual gas atoms are suppressed by filling the cold trap with liquid nitrogen, but some remain. The beam profile monitor indicates the "shape" of the beam by measuring the intensity versus position in the horizontal and vertical planes. Upon entry into the target chamber, the beam encounters a collimator with settings 1/32", 1/8", 1/4" and 5/8" diameter. After the collimator, there is an electron suppression cup operated at -200 V and an isolated shutter used to measure beam current.

In the target chamber, where pressure is less than 1×10^{-6} torr for ion implantation and 6×10^{-8} torr for Rutherford backscattering spectrometry (RBS), there is a four axis goniometer. Samples mounted to this goniometer can be manipulated

with resolution 0.1°. The sample can be rotated, translated ± 1/2" in the horizontal direction, and tilted in the horizontal and vertical directions. A PIPS solid state detector is located at 170° backscattering angle from the incident beam direction for RBS [1]. This detector is covered with a piece of aluminum foil when not in use. Beam current is measured by a charge collection device that has impedance inverse of the full scale of the measured current, meaning that high resistance is needed to measure this very high voltage, low current signal. For RBS, the current is 10-30 nA and for implantation the current is around 1 μA. The signal from the detector passes through a pre-amplifier, which supplies a +50 V bias voltage to the detector, before passing through an amplifier and into a desktop computer with a multi-channel analyzer (MCA). The MCA converts the analog signal to digital and places each count in its corresponding energy bin.

For ion implantation only, the implantation area is determined by implanting a small piece of heat-sensitive paper to a fluence around 1×10^{15} ions cm^{-2}. At this fluence, the paper lightly burns. Uniformity of the implant can be confirmed and the area of the implant can be measured. After burning the piece of paper, the sample is mounted on the same spot and implanted after an appropriate vacuum in the target chamber is reached.

At the University of Houston 1.7 MV tandem accelerator, a He ion beam is made by feeding He gas into a duoplasmatron source. Essentially, it is the same as the 150 kV ion source, with a current flowing from cathode to anode. After extraction from the ion source by electrodes, the positive He beam goes into a canal filled with vporized Li to add electrons. The now negative He beam is accelerated to 60 kV and directed into the mass analyzing magnet. The tandem accelerator is called that because it accelerates the ion beam to the set high voltage twice. In order to receive a 2 MeV He beam, the negative He beam is accelerated by a potential of 920 kV in

the first stage. Between the stages, the beam passes through N gas, which strips the negative He of electrons. In the second stage, the positive He beam is accelerated another 920 kV. The beam energy after all acceleration stages sums to 2 MeV. Finally, the 2 MeV He beam passes through another magnet in order to be directed into the RBS chamber. The RBS chamber possesses a four axis goniometer and a PIPS solid state detector at a 165° backscattering angle. The detector electronics set-up is the same as at Texas A&M University until after the MCA-equipped desktop computer. At Texas A&M University, the desktop computer with MCA card is the final piece of equipment. However, at UH, the MCA is bypassed in favor of a second desktop computer for the purpose of controlling the goniometer for two-dimensional RBS yield mapping, which will be explained in detail later. Proprietary software, written by the UH group, on this second desktop computer controls the goniometer and collects the output data in Microsoft Excel.

CHAPTER II

MOTIVATION

Strained Si technology has been widely adopted in the semiconductor industry over the past several years. Inducing strain in the crystal structure of monocrystalline Si causes favorable changes in semiconducting properties when compared with bulk Si without significantly increasing cost. Previous studies confirm that strained layers amorphize preferentially in a periodic structure consisting of strained and unstrained layers [2, 3, 4, 5, 6]. Deployment of devices made with strained Si technology into extreme radiation environments such as space, nuclear reactors or even aircraft could cause these devices to fail more quickly than bulk Si, which have a long history of use in many different environments. Thus, investigating the radiation tolerance of strained SiGe in comparison with bulk Si experimental control would provide much insight into the suitability of use of strained Si-based devices in harsh radiation environments.

In order to accomplish this, we will cause radiation damage by ion implantation and characterize the implanted samples with Rutherford backscattering spectrometry. The strained layer superlattices to be studied differ in the location of the free surface: the first is 50 nm $Si_{0.8}Ge_{0.2}$/Si and the second is 50 nm Si/60 nm $Si_{0.8}Ge_{0.2}$/Si. The samples were fabricated by molecular beam epitaxy at 650 C.

We will investigate the effect of medium and high energy He ion irradiation into surface and buried strained layers of similar thicknesses on evolution of point defects as well as the stability of strain in strained layers. Defect accumulation and strain stability will be measured simultaneously by the method of RBS angular scanning about the $\langle 110 \rangle$ axis. Additionally, we will use low energy Ag cluster ions to determine if strain causes a fundamental difference in the path to amorphization. High

depth resolution measurements of the defect accumulation caused by cluster ion bombardment will be accomplished by collecting RBS channeling energy spectra of the surface normal axis with a 300 keV He analyzing beam.

CHAPTER III

STRUCTURE, PROPERTIES AND FABRICATION OF SILICON-GERMANIUM STRAINED LAYER SUPERLATTICES

The advantageous properties, the structural changes that cause the properties, as well as the methods of fabrication of strained layer superlattices will be discussed.

A. Structure of Compressively In-Plane Strained Monocrystals

A $Si_{1-x}Ge_x$ layer grown on a bulk Si substrate with (100) orientation so that the crystal structure of the substrate extends into the alloy layer will experience compressive strain in the plane of the substrate surface and tensile strain in the direction of the surface normal [7, 8]. The alloy layer will take the same parallel lattice spacing, $a_{\parallel}$, as the substrate despite the lattice mismatch between Si and Ge, inducing compressive strain in the surface layer. In the direction perpendicular to the surface plane, the layer will relax so that $a_{\perp}$ is greater than that of the substrate.

Fig. 2 shows a side view of the strained layer grown on top of a bulk layer. The parallel lattice spacing is perpetuated in the alloy layer, but the perpendicular lattice spacing expands to balance the compressive strain induced by the substrate.

In this study, the out-of-plane, tensile strain will be quantified by measuring the shift in the angle of an off-normal axial direction. In the case of the $\langle 110 \rangle$ axis in a diamond face centered cubic crystal structure, out-of-plane strain will be exhibited by a deviation of the axis from its normal location of 45°. For tensile out-of-plane strain, the $\langle 110 \rangle$ axis is less than 45°, shifting the off-normal axis closer to the outward surface normal direction. Strain will be determined by comparing the values of d_{0Si} and $a_{\perp}$. The following equation will be used to determine strain:

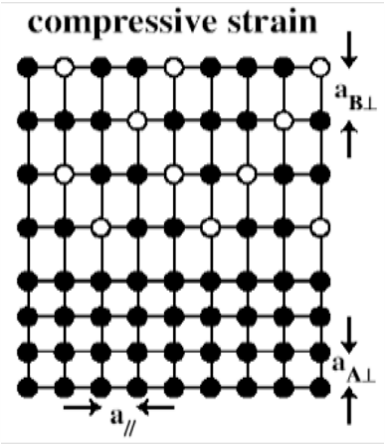

Fig. 2. Schematic of cross-sectional view of substrate with perpendicular lattice spacing $a_{A\perp}$ (black dots) with compressively in-plane strained alloy layer (black and white dots) with relaxed perpendicular lattice spacing $a_{B\perp}$ grown on surface. The parallel lattice spacing $a_{\parallel}$ is the same in strained and bulk layers.

$$\epsilon = \frac{l - l_0}{l_0} = \frac{a_\perp - d_{0Si}}{d_{0Si}} = \tan(45 - \Delta\theta) - 1 \tag{3.1}$$

where $d_{0Si} = a_{\parallel} = 0.5431\ nm$ is the in-plane lattice spacing, $a_\perp$ is the out-of-plane lattice spacing, and $\Delta\theta$ is the shift in the position of the $\langle 110 \rangle$ axis caused by strain. For tensile out-of-plane strain, $\Delta\theta$ is negative and $a_\perp > d_{0Si}$. An illustration of the relationship of $a_\perp$ and $\Delta\theta$ is shown in Figure 3. A tensile strain of 1% corresponds to $\Delta\theta = -0.29°$.

1. Analysis of Structure by Rutherford Backscattering Spectrometry

From the point of view of ion beam analysis, which will be used to characterize radiation damage in this study, this shift from a diamond-like cubic crystal structure to a diamond-like tetragonal crystal structure wil be utilized to determine shifts in strain. This will be discussed in detail in subsection 4 of the next chapter.

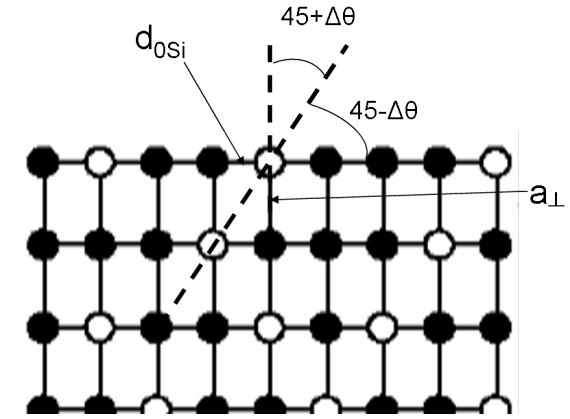

Fig. 3. Illustration of the values $\Delta\theta$, which will be measured experimentally, and $a_{\|}$. This value will be used to determine strain by Eq. 3.1.

B. Property Changes in Strained Layers

Strain changes the electronic band structure that leads to improvements in both the band gap and carrier mobilities. According to Figure 4(a), in-plane compressively strain in SiGe will shift both the conduction and valence bands to higher energy, but the bandgap will decrease because the valence band shifts much more than the conduction band. According to Figure 4(b), in-plane tensile strain in Si and SiGe will also shrink the bandgap. In-plane tensile strain in Si will cause the k-space, or electron scattering, to lose symmetry, as shown in Figure 5. The k-space decreases in-plane, and increases out of plane. This change induced by strain can mean that electron mobility increases by a factor of two and hole mobility by one order of magnitude.

C. Fabrication of Strained Layer Superlattices

The two methods of fabricating high purity and highly textured SiGe layers are molecular beam epitaxy (MBE) and chemical vapor deposition (CVD). Controlling impurities is very important in both processes. In MBE, the growth chamber must be at ultra-high vacuum to suppress impurities. In CVD, the reactor must be at ultra-

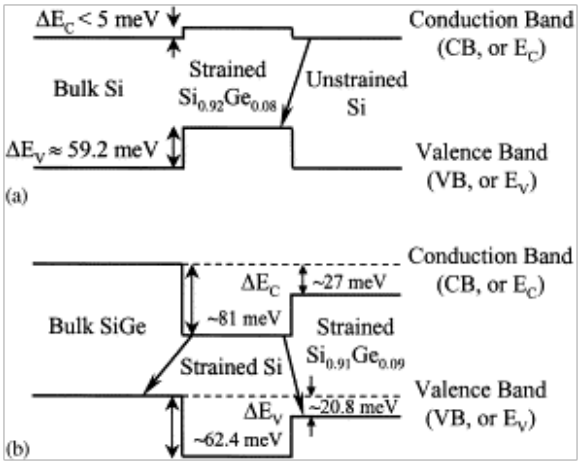

Fig. 4. Shift in conduction band and valence band induced by strain for strained layers grown on (a) bulk Si and (b) relaxed SiGe shown in Figure 6 [9].

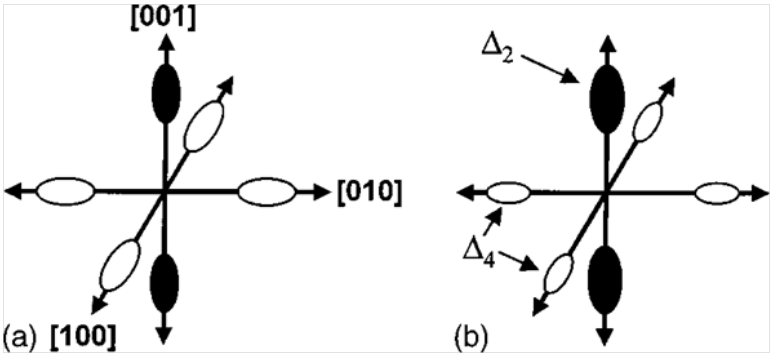

Fig. 5. The k-space, or electron frequencies that can be scattered, changes from six-fold symmetry in bulk Si to four-fold in-plane symmetry and two-fold out-of-plane symmetry in strained Si. The area of the Brillouin zones decreases in-plane, meaning that fewer electron frequencies can be scattered, increasing in-plane carrier mobility. More electron frequencies can be scattered in the out-of-plane direction. This combined effect increases electron mobility by up to a factor of two [10].

high vacuum and/or the reactant gases must be highly purified. The absorption of O in SiGe is much greater than in Si grown by CVD methods, therefore impurities must be tightly controlled.

1. Growth by Molecular Beam Epitaxy

Molecular beam epitaxy is a process characterized by extremely low growth rates, where atoms adsorb on the surface of the substrate and arrange themselves into the crystal structure of the substrate. This can only be accomplished with the sample at elevated temperature, in our case 650 C, and the substrate temperature must be uniform across the surface and well controlled throughout the growth process. The maximum growth rate in the MBE system used to grow the samples investigated in this study is 1 nm/second. This growth method is sensitive to impurities, so it must be carried out at ultra-high vacuum [11].

2. Growth by Chemical Vapor Deposition

Strained layer Si/SiGe superlattices can be grown by ultra-high vacuum chemical vapor deposition (UHV-CVD) using purified silane and germane gases on bulk Si and relaxed $Si_{1-y}Ge_y$ substrates [9]. The samples in Figure 6 were grown at 525 C in a commercially available reactor. For industrial fabrication, CVD has high efficiency and lower cost than MBE.

3. Critical Thickness of Strained Layers

If a strained layer is grown too thick, it will relax by forming dislocations at the interface of strained and unstrained layers [12]. In this manner, the difference in the parallel and perpendicular lattice spacings will approach zero and strained layer will relax. To obtain a film with high Ge concentration, multiple thick buffer layers

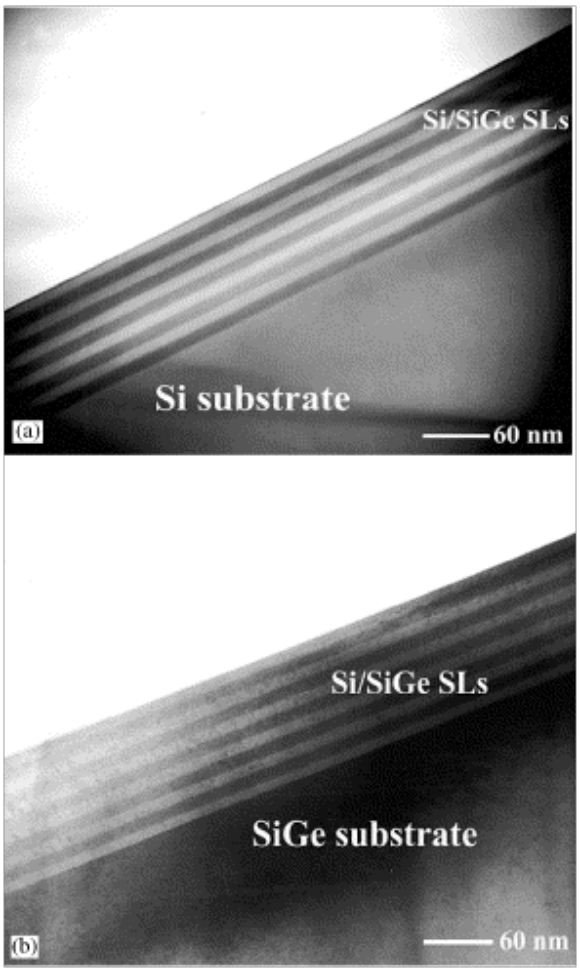

Fig. 6. Cross-sectional transmission electron micrographs of (a) 5 periods of 10 nm Si/12 nm $Si_{0.92}Ge_{0.08}$ superlattice grown on (100)-oriented n-type bulk Si and (b) 5 periods of 10 nm strained Si/15 nm $Si_{0.91}Ge_{0.09}$ grown on relaxed $Si_{0.86}Ge_{0.14}$ substrate by ultra-high vacuum chemical vapor deposition (UHV-CVD) [9].

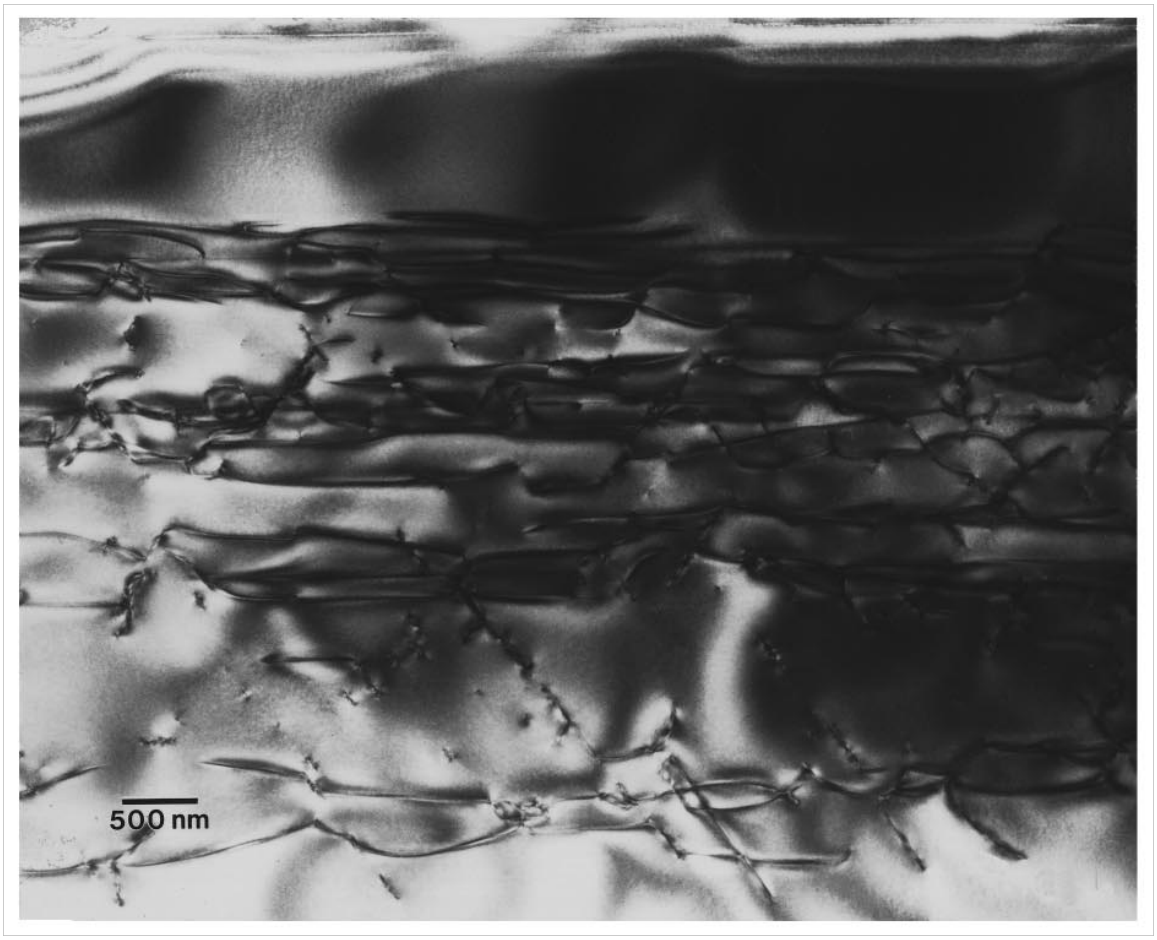

Fig. 7. Misfit dislocations in thick relaxed $Si_{1-y}Ge_y$ virtual substrates [13].

with increasing Ge content are grown. The thickness and high Ge content cause strain relaxation by misfit dislocation generation at the interfaces of graded layers, as shown in Figure 7.

CHAPTER IV

RUTHERFORD BACKSCATTERING SPECTROMETRY

The existence of the nuclear structure of the atom was proven in 1913 by Geiger and Marsden while working for Ernest Rutherford. A well-collimated beam of alpha particles was made to impinge on a Au foil so that the angular dependence of scattering of alpha particles from the Au foil could be determined [14]. Rutherford backscattering spectrometry remains a prominent materials tool to characterize almost any solid material to this day. It is valuable for determining the depth dependence of elemental concentrations in the near-surface region of a solid material. If the material is monocrystalline, displacement data can also be extracted. Backscattered He atoms are recorded as counts and placed into the energy bin interval containing their detected energy. The data in a RBS spectrum is counts per channel as a function of channel number, which is proportional to energy of backscattered beam particles. The counts per channel is proportional to the areal density of atoms of a specific mass that the ion interacted with in the sample, and thus data on the concentration of elements can be obtained.

RBS is performed in a vacuum chamber with the sample mounted to a goniometer with a solid state surface barrier detector mounted at a backscattering angle from the direction of travel of the beam. Figure 8 shows a schematic of an incoming ion beam impinging on a crystal sample mounted to a goniometer with a solid state detector at a fixed backscattering angle.

A. Energy Loss Due to Elastic Scattering

The atomic mass of the target atom is obtained in Rutherford backscattering spectrometry by determining the energy an incoming particle loses when scattered through

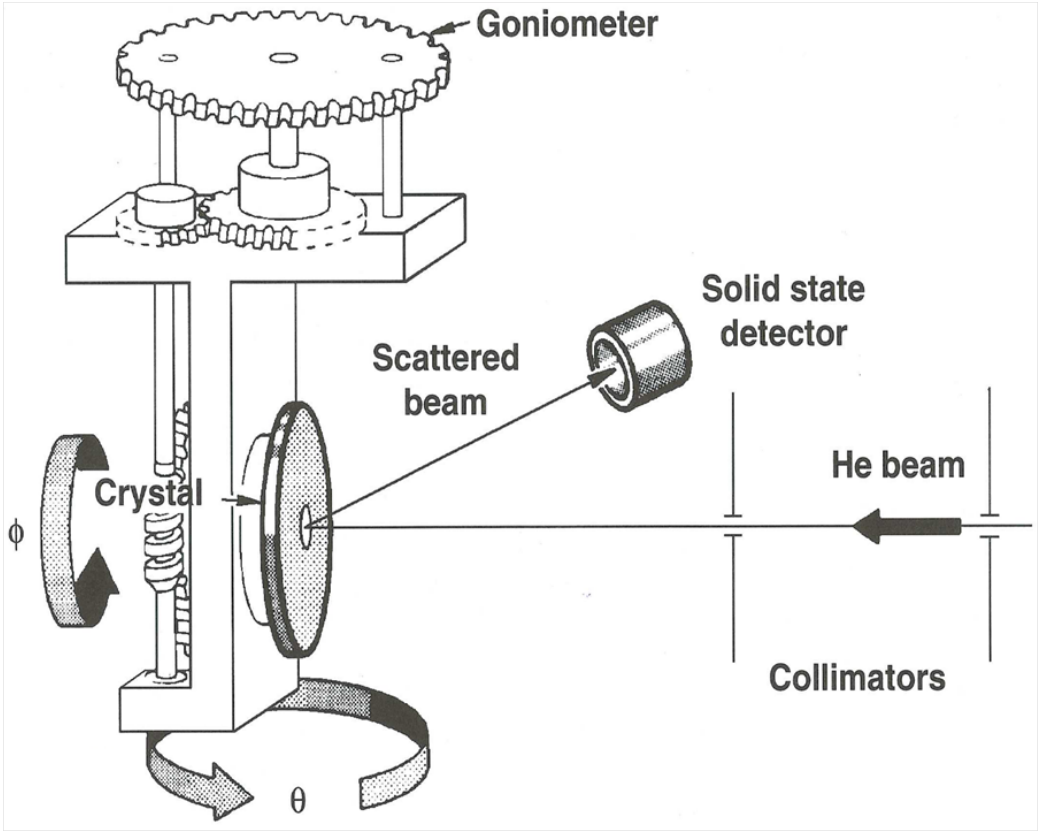

Fig. 8. Schematic of two-axis goniometer and solid state detector from [15]. The two axes are rotation of the sample and tilt along one direction. The energy of ions backscattered through a fixed solid angle is collected by the solid state detector.

a fixed angle. The target atom mass M_2 must be greater than the incoming particle mass M_1 for backscattering to occur.

In the laboratory frame of reference, for any combination of projectile mass, target mass and scattering angle, the ratio of outgoing energy to incoming energy can be found by solving the conservation of energy and momentum equations. Solving in terms of the ratio of scattered ion energy to incoming ion energy gives the equation for the kinematic factor, K,

$$K = \frac{E}{E_0} = \left[\frac{\left(M_2^2 - M_1^2 \sin^2 \theta \right)^{1/2} + M_1 \cos \theta}{M_1 + M_2} \right]^2 \tag{4.1}$$

where E is the energy of the ion entering the detector, E_0 is the energy of the incoming ion beam, θ is the angle through which the ion is scattered in the laboratory frame of reference, and M_1 and M_2 are the masses of the projectile and target atoms, respectively [16].

Values for the kinematic factor K are tabulated in [14] and [16] as functions of projectile mass, target mass and backscattering angle so that calibrations can be made to accurately determine the relation of output channel to energy.

In practice, RBS is best suited for detection of heavy elements in the near-surface region of a light substrate. In a thick target, the backscattering signal from beam atoms penetrating deeply into the substrate before scattering will obscure the signal of elements with lower atomic mass than the substrate. High concentrations of light elements on the surface of a sample will be observed in the RBS energy spectrum, but this signal will be rendered unusable by the large background contributed by the substrate.

B. Channeling RBS

Aligning the ion beam with a major crystalline axis in a monocrystalline material will cause the backscattering yield of incoming ions to decrease by approximately two orders of magnitude because of the steering effect of the rows of atoms. Alignment of the ion beam with a crystal plane will also cause a reduction of backscattering yield, though this reduction will be less than in the case of axial channeling. When the beam hits the surface of a material, the fraction of the beam that has trajectory unsuitable for channeling is scattered away. Backscattering yield is reduced by the focusing of ions by small-angle forward scattering with the electronic potential of the rows of atoms. After the beam is focused by this phenomenon, dechanneling of ions is primarily caused by defects. The number of permanently displaced atoms in a crystal can be determined as a function of depth by this method.

1. Angular Scanning

The width of the axial channel can be found by plotting counts from the surface region as a function of tilting angle. The ion beam must be aligned with the crystalline axis within a value called the half-angle $\Psi_{1/2}$ for channeling of the ion beam to occur [17]. This value can be calculated for any combination of incoming particle, target atom and crystalline axis by the equation

$$\Psi_{1/2} = \sqrt{\frac{2Z_1 Z_2 e^2}{Ed}} \tag{4.2}$$

where Z_1 and Z_2 are the atomic numbers of the incoming ion and target atoms, respectively, E is the energy of the incoming ion in MeV, d is the atomic spacing along the crystalline axis being probed in angstroms and the value is given in units

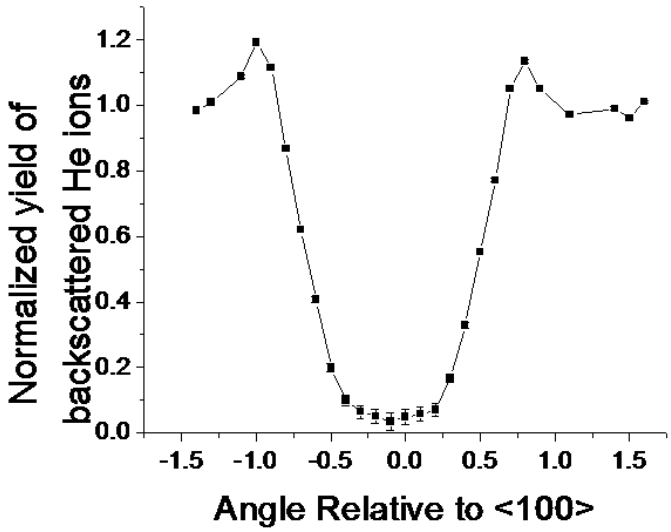

Fig. 9. Backscattering yield from the near-surface region as a function of tilt angle across the $\langle 100 \rangle$ axis in bulk Si. The half-angle $\Psi_{1/2}$ is half of the full-width half-maximum of the dip.

of degrees [14].

Figure 9 shows the normalized yield of 2 MeV He ions backscattered from the near-surface region of bulk (100)-oriented Si as it was tilted through the $\langle 100 \rangle$ axis. Counts are plotted as a function of tilt angle, where the inward surface normal is defined as 0°. The sample is rotated so that the tilting of the sample is not parallel to a plane channel, ensuring the beam does not strike a plane channel. As the beam is tilted through the $\langle 100 \rangle$ axis, yield varies according to the alignment of the sample. Far from the axis (a few degrees or more), the sample appears to have no order, so the backscattering yield has no strong dependence on tilt angle. This condition is referred to as "not aligned" or "random". As the beam approaches the axis (within 1–2°), it scans through a portion of maximum areal density, creating a "shoulder" in the yield curve. After the beam scans past this "shoulder" region, yield begins to decrease to values from 1–4% of the yield of the non-aligned portion of the curve,

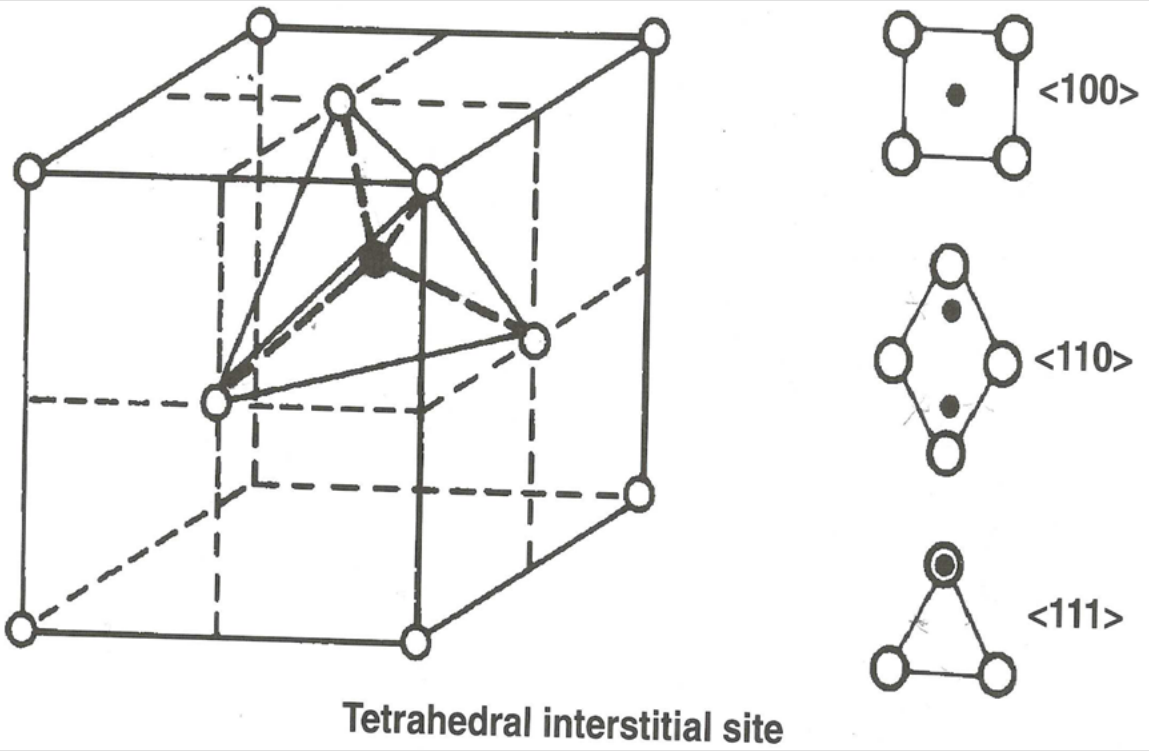

Fig. 10. Position of tetrahedral interstitials and there projection into the ⟨100⟩ axis, ⟨110⟩ axis and ⟨111⟩ axes of a face centered cubic lattice [18].

depending on the energy and species of the projectile and the target, if the target is relatively defect-free.

The position of defects can be determined by the method of angular scanning across different crystalline axes. Preferred orientation of interstitial defects, for example, can be determined by investigation of the the three major axes. Tetrahedral interstitials in a face centered cubic lattice can be found by comparing angular scans of the ⟨100⟩ axis, ⟨110⟩ axis and ⟨111⟩ axes, as shown in Figure 10.

Locations of many types of defects can be inferred by the shape of the angular scan. Figure 11 shows angular scans produced by many types of defects. The solid line shows a "normal" angular scan of a bulk monocrystalline sample with low defect concentration. The angular scan for the given condition is shown by the dotted

line. Figure 11(a)-(d) shows the progression of the angular scan as defects move from perfect substitutional sites to the center of the axis of interest. If the defect distribution is perfectly random, scanning across any angular interval will result in a flat line, as shown in Figure 11(e). Mixing location of defects results in combinations of the expected angular scans shown in 11(a)-(d). Figure 11(f) and (g) show two such conditions.

Figure 12 is a polar plot of the planes and axes of bulk Si with (100) orientation. The origin is the ⟨100⟩ axis, with the ⟨110⟩ axis 45° off-normal and the ⟨111⟩ 54° off-normal. There are many axes in Si, but these three have the largest half-angles because they have the largest atomic spacing.

The axes of interest in this study are the ⟨100⟩ axis and ⟨110⟩ axis in the diamond face centered cubic structure. The surface normal of the samples under investigation is the ⟨100⟩ axis. Therefore, the ⟨110⟩ axis is an off-normal axis. Axes are formed by the intersection of multiple crystal planes, and the intersections of crystal planes in the ⟨100⟩ and ⟨110⟩ axes are shown in Figures 13 and 14.

2. Random and Channeled Energy Spectra

In the method of angular scanning, the counts in a narrow window of backscattering energy are integrated and plotted as a function of sample tilt angle. However, if the sample is fixed, counts will be plotted as a function of backscattering energy. Comparing the counts per channel of a spectrum obtained with the beam in channeled mode, well-aligned with a crystal axis, to that with the beam not aligned will give the depth dependence of crystalline imperfection. This method is particularly useful for quantifying damage caused by ion irradiation near the sample surface because of the well-defined range of ions in a solid material.

Backscattering yield can be decreased by up to two orders of magnitude by

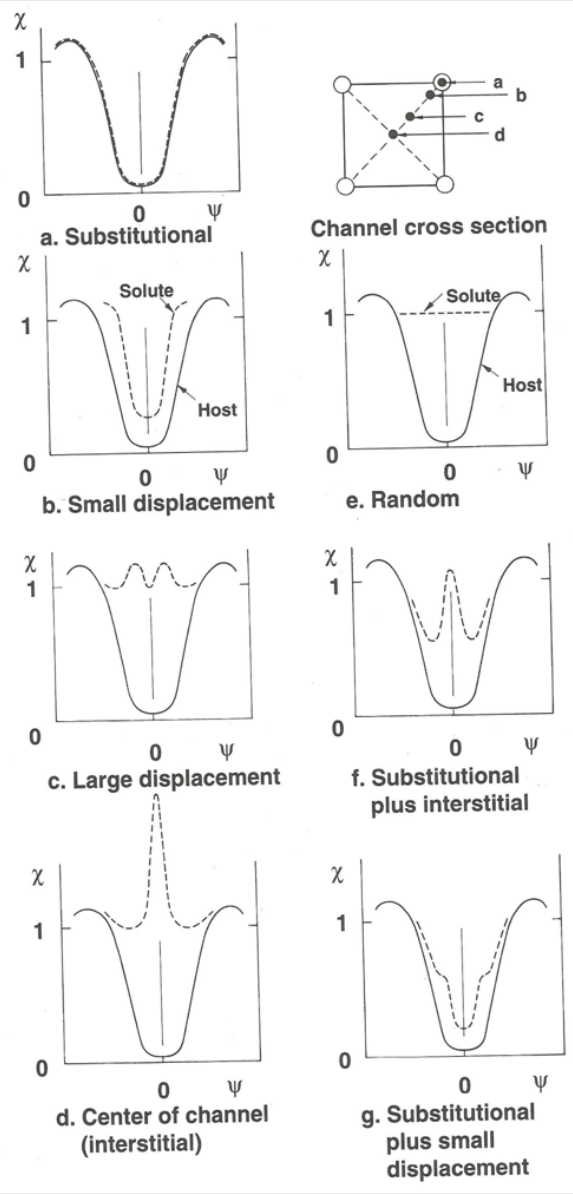

Fig. 11. Changes in angular scans based on different defect distributions. The solid line shows an angular scan from a bulk sample with low defect concentation, and the dotted line shows the expected change in the angular scan due to the specified condition. Scans (a)-(d) show the effect of position of interstitial defect in the axis of interest. Scan (e) shows the result of isotropic distribution of defects. Scans (f) and (g) show the expected result of multiple defect configurations. This figure adapted from [19].

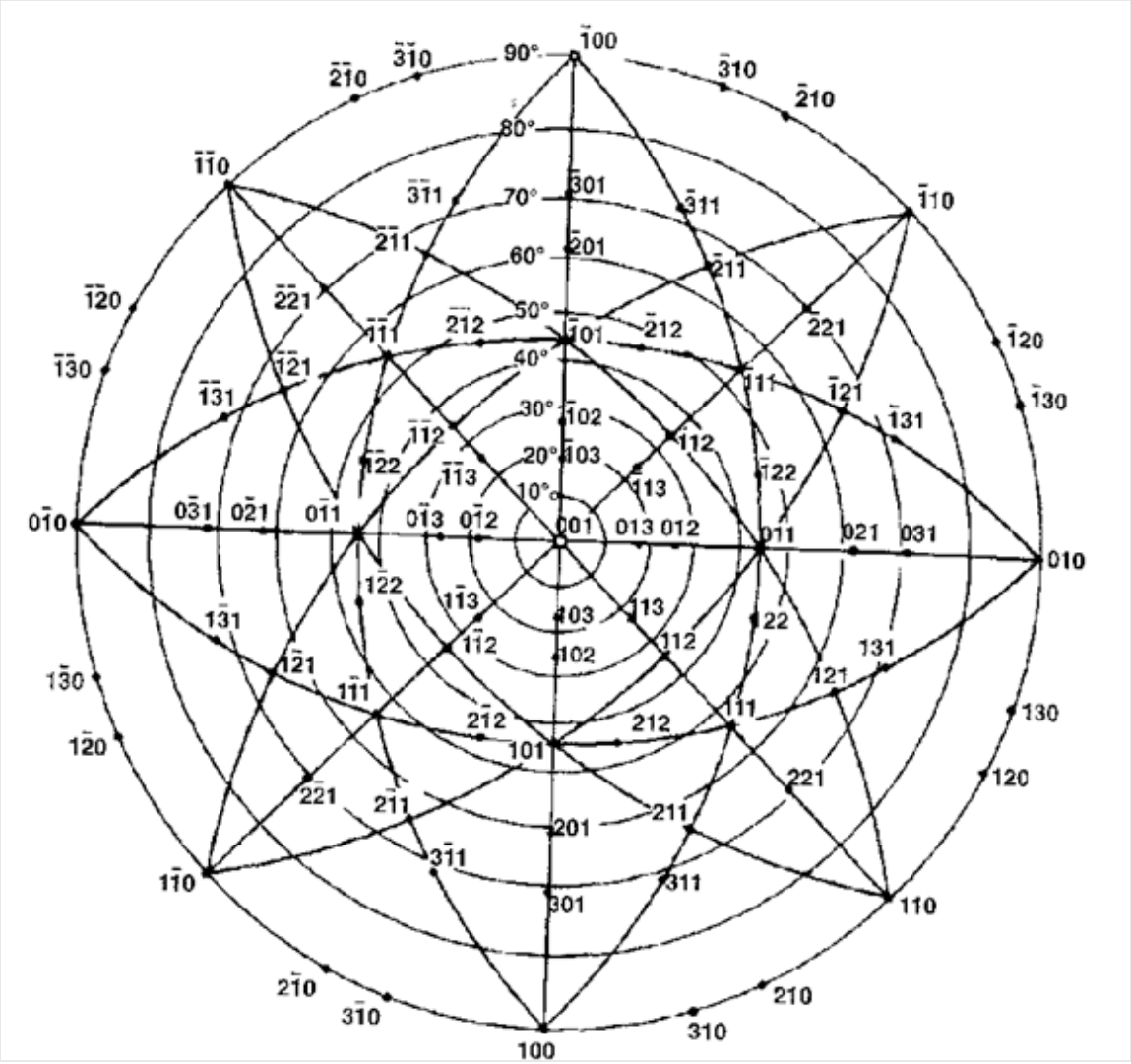

Fig. 12. Polar plot of (100)-orientation Si, where lines are crystalline planes and the points of intersection of one or more lines are crystalline axes [16].

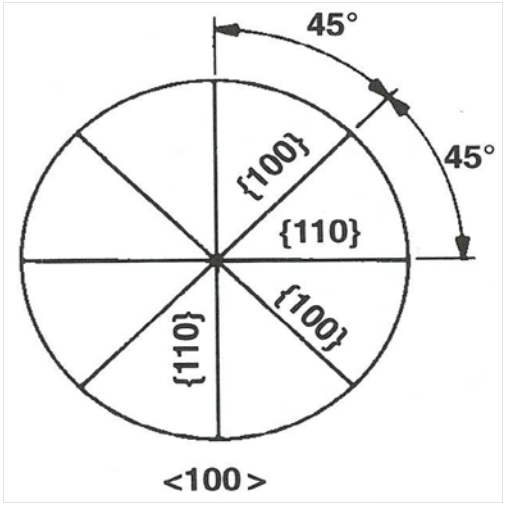

Fig. 13. The ⟨100⟩ axis and intersecting planes, from [16].

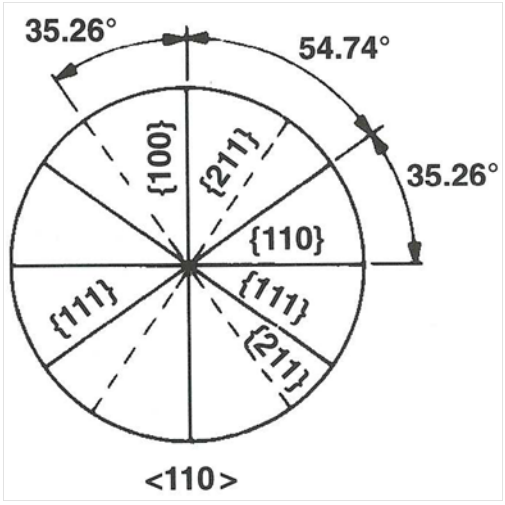

Fig. 14. The ⟨110⟩ axis and intersecting planes, from [16].

aligning the ion beam within the critical angle of a crystal axis in a sample with low defect concentration. Figure 15 shows random and channeled energy spectra measured from the ⟨100⟩ axis of monocrystalline W with 2 MeV He analyzing beam. The ideal random spectrum is a box, so 2 MeV He impinging on W approaches the ideal case in the energy region shown. At lower energies not shown in Figure 15, the tail of the random energy spectrum increases due to noise caused by overlap of counts. At the highest energy in the channeling spectrum, there is a peak in the backscattering yield. This is created by interaction of incoming He ions not suitable for channeling with W atoms on the surface of the sample, and is labeled the surface peak. Beyond the surface, in the near surface region, backscattering yield from the well-aligned beam is low. This is the depth region that should be studied by this method. Different combinations of ion species, ion beam energy, sample and desired information dictate different analysis conditions. Lower beam energy increases depth resolution and critical angle, but the depth of analysis is decreased. Lower beam mass increases the depth of analysis at the expense of target mass resolution. Analysis conditions must be carefully chosen in order to gather the desired data.

3. Displacement Ratio

Characterization for experiments aimed at understanding the evolution of defect accumulation in monocrystals can be carried out by comparing channeling yield in a sample to channeling yield of a control sample, unaltered by experiment. The channeling yield, χ, is the ratio of the counts in the same channel of aligned and non-aligned energy spectra,

$$\chi = \frac{C^i}{\overline{C}_R} \tag{4.3}$$

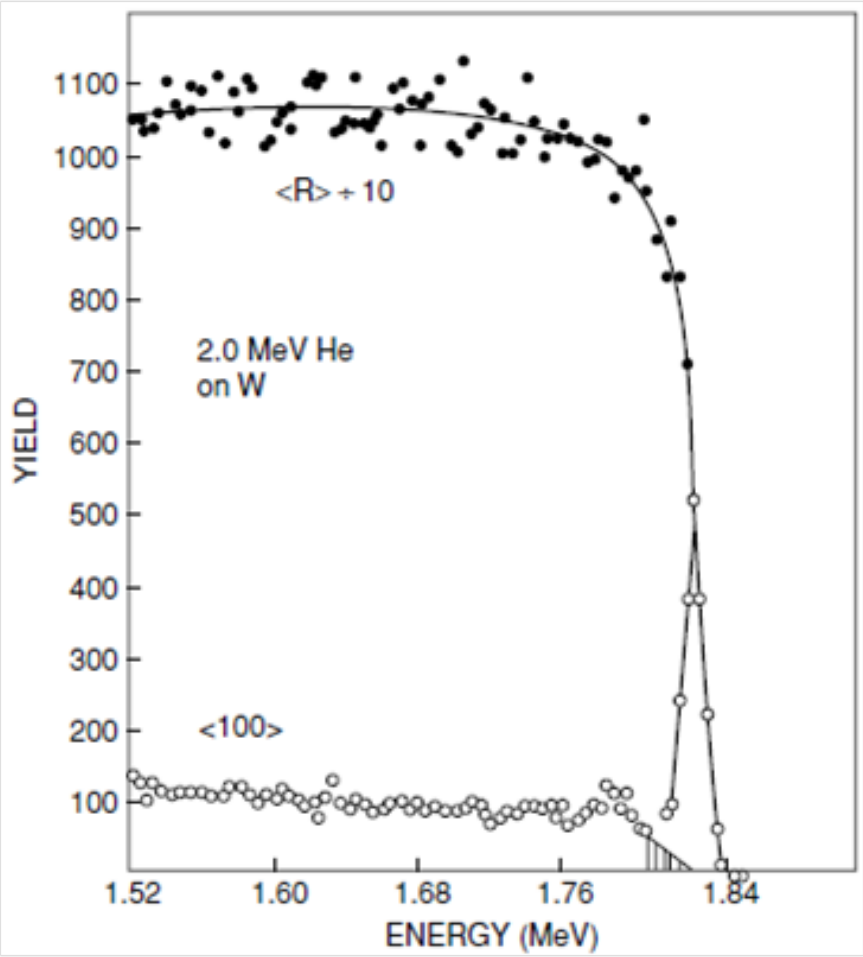

Fig. 15. Random (filled circle) and channeled (open circle) backscattering energy spectra from a 2 MeV He beam aligned with the ⟨100⟩ axis of W, from [20]. The counts of the random spectrum have been reduced by a factor of 10.

where C^i is counts in channel i in an aligned energy spectrum and C_R^i is counts in channel i in a non-aligned, random energy spectrum. For the control sample, unaltered by experiment, the channeling yield should be 1–4%, as stated in Subsection 1. The permanent displacement ratio, n_D/n, in the axis being analyzed can be expressed as

$$\frac{n_D}{n} = \frac{\chi_E^i - \chi_V^i}{1 - \chi_V^i} = \frac{C_E^i - C_V^i}{C_R^i - C_V^i} \tag{4.4}$$

where superscript i is the channel in all spectra, subscripts E and V refer to channeling spectra from experimental samples and control, virgin samples, subscript R refers to random spectrum, χ refers to channeling yield and C^i refers to counts in channel i as described in equation 4.3.

4. Measuring Strain by Angular Scanning

Strain can be measured with RBS determining the shift in location of axis in strained and unstrained layers. Out-of-plane strain in (100)-oriented Si can be measured by comparing the locations of the $\langle 110 \rangle$ axis in strained and bulk layers. Out-of-plane strain in any monocrystal with any orientation can be measured by comparing the location of an off-normal axis in strained and unstrained layers. The difference in angle of tilt location of an off-normal axis caused by strain is called the kink angle. In a strained layer superlattice with tensile out-of-plane strain, the kink angle is such that the off-normal axis is shifted closer to the normal axis. A schematic of the geometry of a sample with tensile out-of-plane strained layer is shown in Figure 16 [21].

A schematic of periodic strained/unstrained GaSb/AlSb sample is shown in Figure 17. The dechanneling probability is not uniform across the channel as the ion

beam passes through interfaces between strained and unstrained layers. The structure shown in Figure 17 was simulated by a three-dimensional kinetic Monte Carlo simulation and the backscattering probability as a function of depth into the sample is shown in Figure 18. Clearly, the backscattering yield is most asymmetric at the first interface and continues to be asymmetric as depth increases. This results in a "damping" of the location of the channeling axis, as shown in Figure 19. As the ion beam navigates an increasing number of interfaces, the ion beam comes into equilibrium, meaning that it can be steered by the alternating layers without significantly increasing backscattering yield.

5. Two-dimensional Backscattering Yield Mapping

The method of two dimensional backscattering yield mapping is based on expanding the methodology of angular scanning such that backscattering yield can be mapped as a function of position in the tilt plane. A backscattering yield map consists of many stereographically parallel angular scans about a chosen channeling axis. In this experiment, the method of selecting the backscattering energy window remains the same as in traditional angular scanning; that is to say, a relatively large energy window is chosen and counts within that energy window are integrated and plotted.

Figure 20 shows a two-dimensional backscattering yield map of the $\langle 110 \rangle$ axis in (100)-orientation bulk Si [23]. The $\langle 110 \rangle$ axis is symmetric, and four major plane channels that intersect to form the $\langle 110 \rangle$ axis are visible. The horizontal plane channel is $\{100\}$, the vertical $\{110\}$, and the other two major planes are $\{111\}$ planes. Additionally, two $\{211\}$ planes are visible, though they are not resolved as well as the major planes.

For angular scans of an off-normal axis to appear parallel, a coordinate transformation must be applied so that the ion beam traces across projections of parallel lines

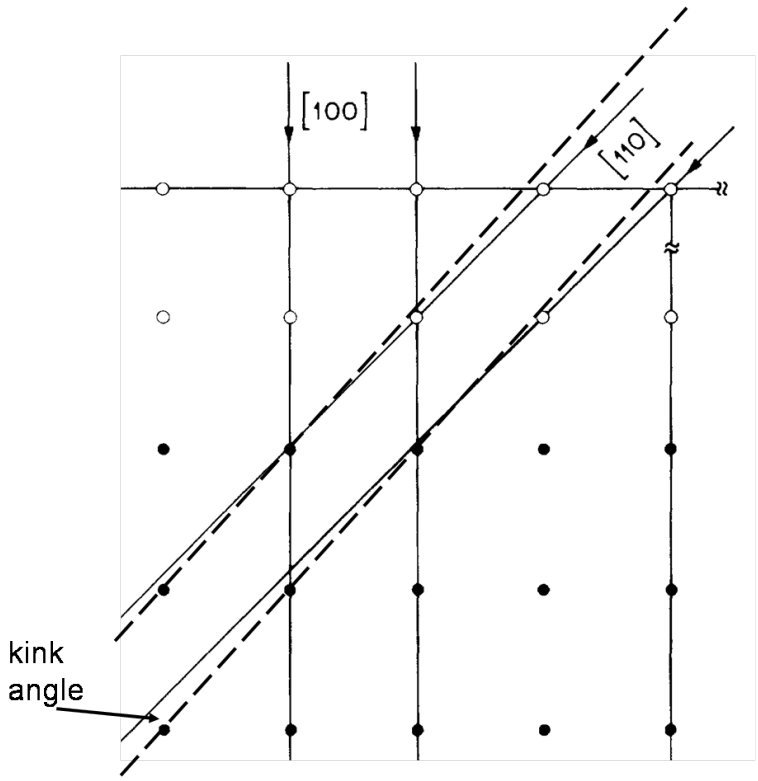

Fig. 16. Illustration of shift of axis location as a function of strain in the layers of a strained layer superlattice [21]. The perpendicular lattice spacing in the layer composed of black dots is greater than in the layer composed of white dots. The "kink angle", the difference in the tilt position of the off-normal axes in strained and unstrained layers, is denoted.

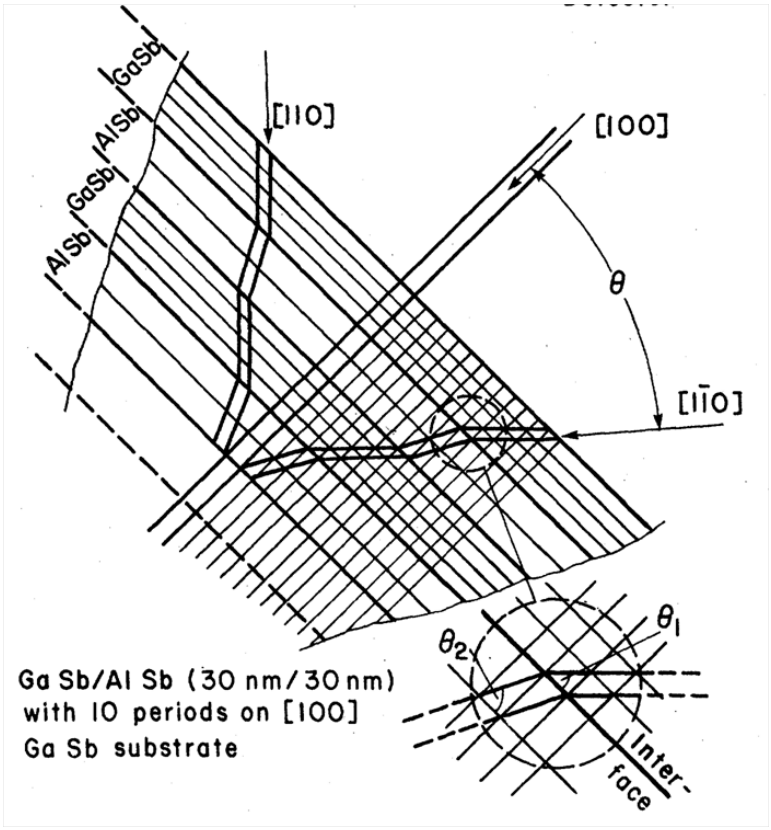

Fig. 17. A schematic representation of two periods of GaSb/AlSb showing the mismatch in off-normal axes created by tensile out-of-plane strain in one layer in each period [22].

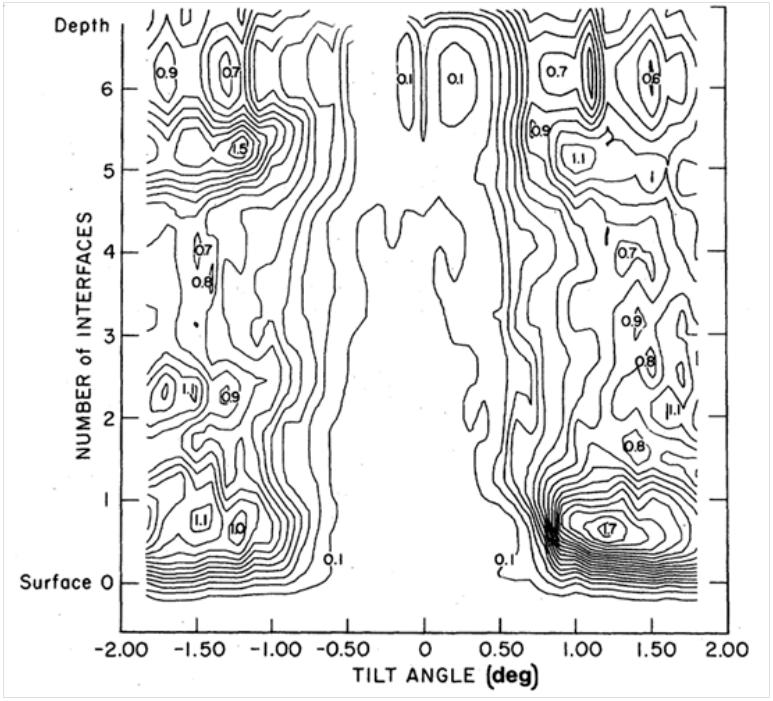

Fig. 18. Normalized backscattering probability calculated by kinetic Monte Carlo simulation for 2 MeV incident He particle as it traverses the strained layer superlattice in Figure 17 [22].

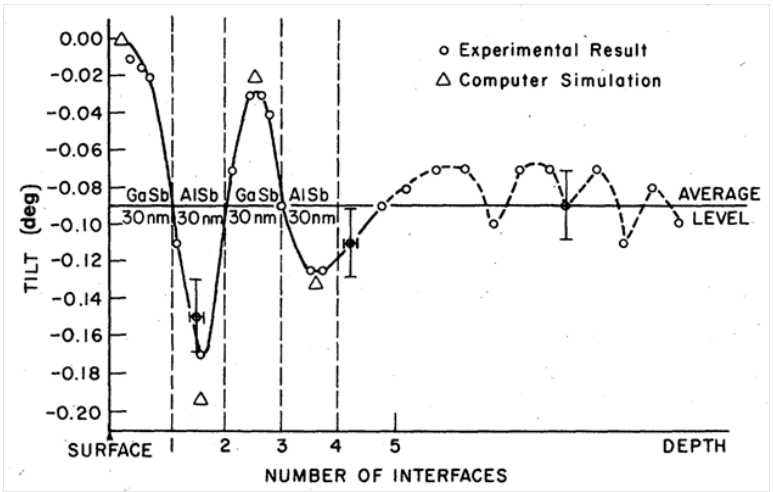

Fig. 19. Reduction in measured kink angle due to equilibration of analyzing beam caused by beam focusing in the channeling axis [22].

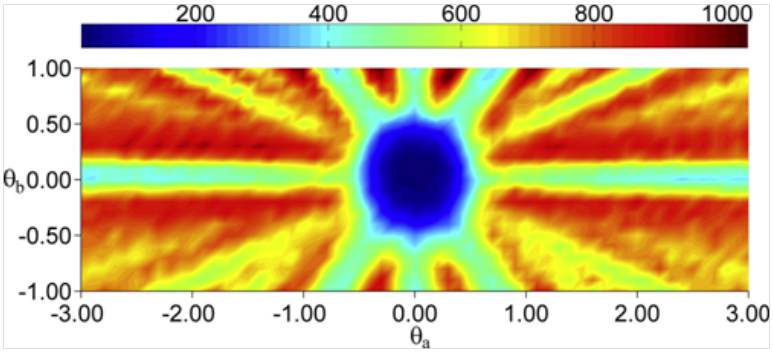

Fig. 20. Two dimensional backscattering yield map of ⟨110⟩ axis in (100) orientation bulk Si [23].

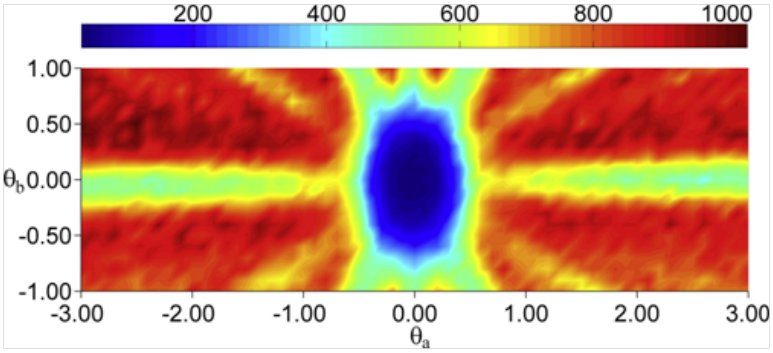

Fig. 21. Two dimensional backscattering yield map of ⟨110⟩ axis in (100) orientation bulk Si without the proper transformation to ensure angular scanning projections are parallel to each other [23].

from its perspective. This coordinate transformation can be applied before or after collection of the angular scans. However application of the transformation after data collection will cause the tilt angle mesh to be non-uniform, and for the map of the backscattering yields to be oddly shaped. Without any coordinate transformation, the map will appear distorted and the axis will no longer appear round.

Figure 21 shows mapping of the same axis shown in Figure 20 without coordinate transformation. Lacking this transformation, angular scans trace a trapezoid with the lines diverging with increasing horizontal and vertical tilt angles. Distortion and loss in symmetry is caused by this phenomenon.

CHAPTER V

DISPLACEMENT ACCUMULATION IN ION-IRRADIATED BULK SI AND SURFACE STRAINED SILICON-GERMANIUM LAYER

Displacement accumulation caused by 140 keV He irradiation will be measured by Rutherford backscattering spectrometry with a 140 keV He beam. Analysis will be carried out by scanning the ⟨110⟩ crystal axis along the [100] plane. Measurement of this kind can serve two roles: minimum yield gives displacement data, and shift in the location of minimum yield will indicate any change in strain.

A. Experimental Procedure

The sample under investigation is a strained layer superlattice (SLS) consisting of 50 nm $Si_{0.8}Ge_{0.2}$ surface layer on top of 200 nm Si buffer layer grown on 6" (100)-oriented Si wafer by low temperature molecular beam epitaxy. Bulk Si with (100) orientation was used as the control sample in this study. The samples were irradiated with 140 keV He^+ ions to fluences ranging from 9×10^{15} to 6×10^{16} ions cm^{-2}. For irradiation steps, the ion beam was rastered over the sample and the sample was randomly oriented to the ion beam. However, for the sake of preserving the implantation area between steps, the beam was not deflected to minimize irradiation by ions that become neutral during flight from the source to the target. Thus, the fluences reported are an underestimation.

After each irradiation, an angular scan of the ⟨110⟩ axis was taken to determine displacement accumulation. A PIPS detector located at 170° backscattering angle with resolution estimated to be 14 keV was used to collect backscattered He signal. In total, seven angular scans across the tilt angle interval from 38° to 52° by the low current analyzing beam and six implantations by the high current irradiation

beam were performed. The ion fluence required for each angular scan was minimized to reduce displacement accumulation caused by the analysis beam. The beam spot size for ion irradiation was 1 cm^2 and for analysis 2 mm^2. Angular scans along the $\langle 100 \rangle$ and $\langle 111 \rangle$ axes were performed after ion irradiation to an intermediate fluence to determine if a specific configuration of displacements exist in strained surface $Si_{0.8}Ge_{0.2}$ surface layer.

The "box" method for aligning the beam with the sample is used to initially align the sample's surface normal with the incoming ion beam, and is discussed in detail in A.

B. Results and Discussion

Figure 22 shows angular scans through $\langle 110 \rangle$ axis of $Si_{0.8}Ge_{0.2}$ surface layer with increasing ion fluence. Backscattering yield shows a strong dependence on ion fluence, increasing with each fluence step shown. Figure 23 shows the angular scans from bulk Si subjected to the same irradiation and analysis conditions as in Figure 22. The minimum yield is much lower after high fluence radiation of bulk Si compared to strained SiGe. Backscattering yield, χ is obtained by dividing the counts in each channel (angular step) by the counts from the random portion of the angular scan as in Equation 4.3.

The change in tilt angle in each channel in Figure 22 is around 0.2°, and though it might appear that the location of the $\langle 110 \rangle$ axis increases, the coarse angular tilt step makes it impossible to definitively conclude that strain decreases.

The permanent displacement ratio can be calculated by Equation 4.4 for the 140 keV He irradiated samples, and this data is shown in Figure 24. The number of permanently displaced atoms in strained surface $Si_{0.8}Ge_{0.2}$ layer increases linearly

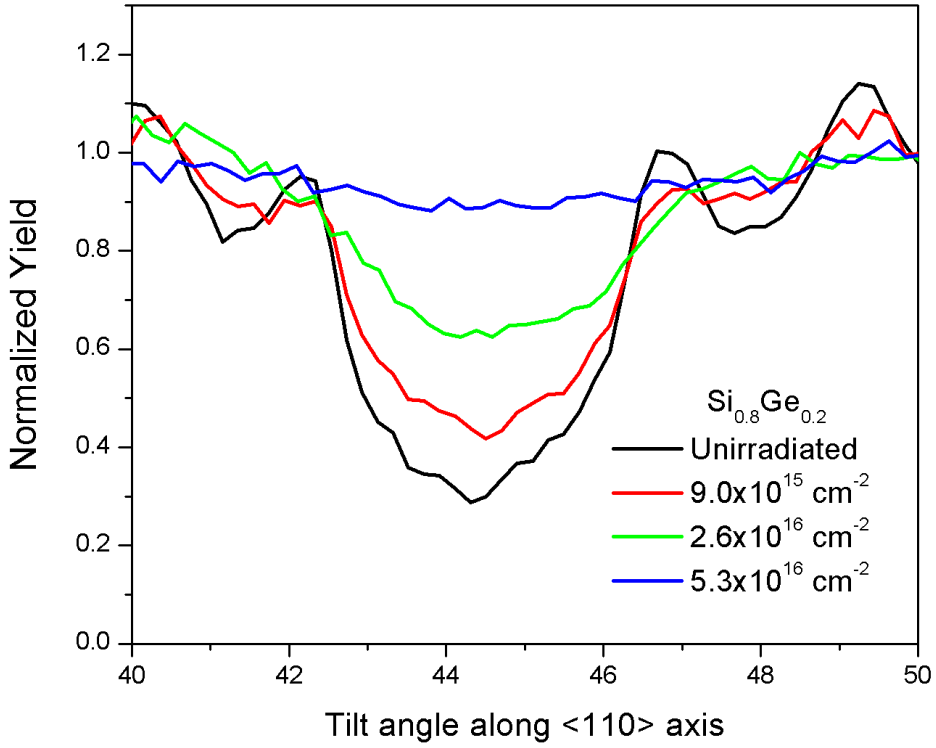

Fig. 22. RBS angular scans of $\langle 110 \rangle$ axis of $Si_{0.8}Ge_{0.2}/Si$ after irradiation by 140 keV He ions to specified fluences [24].

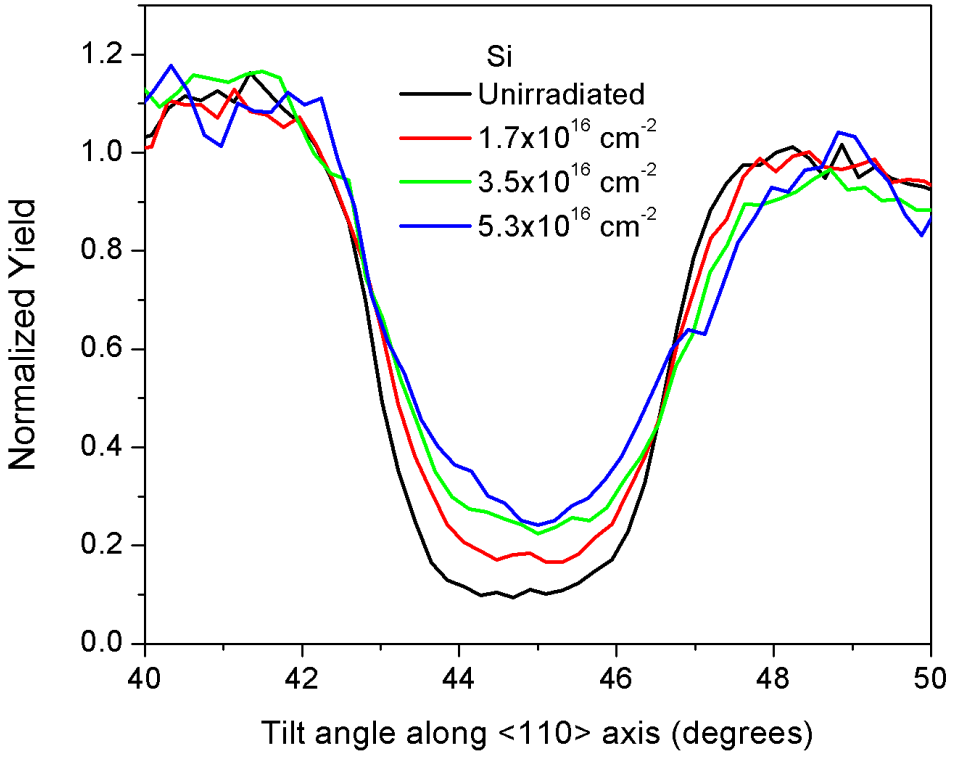

Fig. 23. RBS angular scans of ⟨110⟩ axis of bulk Si after irradiation by 140 keV He ions to specified fluences [24].

with increasing ion fluence, whereas the number of permanently displaced atoms in bulk Si appears to remain unchanged.

Irradiation by energetic ions causes atomic displacements, creating interstitial (I) and vacancy (V) point defects. Points defects can be trapped by other defects through the processes of I-V recombination or nucleation or growth of higher-order defect clusters. The recombination of point defects in bulk Si appears to reach steady state compared with the production of point defects. If we assume that the production of interstitials and vacancies in strained SiGe and bulk Si is similar, the kinetics of defect production or defect recombination must differ. The path to amorphization of strained SiGe and bulk Si will be investigated in the next chapter, so we shall limit ourselves to the discussion of point defect kinetics in the remainder of this chapter.

For room temperaure irradiation with light ions, it can be assumed that the dominant defects remaining after quenching of the ion track are point defects. Under these assumptions, the time evolutions of concentration of interstitials and vacancies are equivalent, and can be described by the equation

$$\frac{dC_{I,V}}{dt} = P_{I,V} - 4\pi r e^{-\frac{E}{kT}} C_I(t) C_V(t)(D_I + D_V) \tag{5.1}$$

where $C_{I,V}$ is concentration of interstitials or vacancies, $P_{I,V}$ is the production of interstitials or vacancies by He ion irradiation, r is the I-V recombination radius, k is Boltzmann constant, T is effective temperature of the bulk (including heating by ion irradiation), E is the energy barrier for I-V recombination and $D_{I,V}$ is the diffusivity of point defects.

Equation 5.1 suggests that a steady state in the concentration of point defects can be reached when

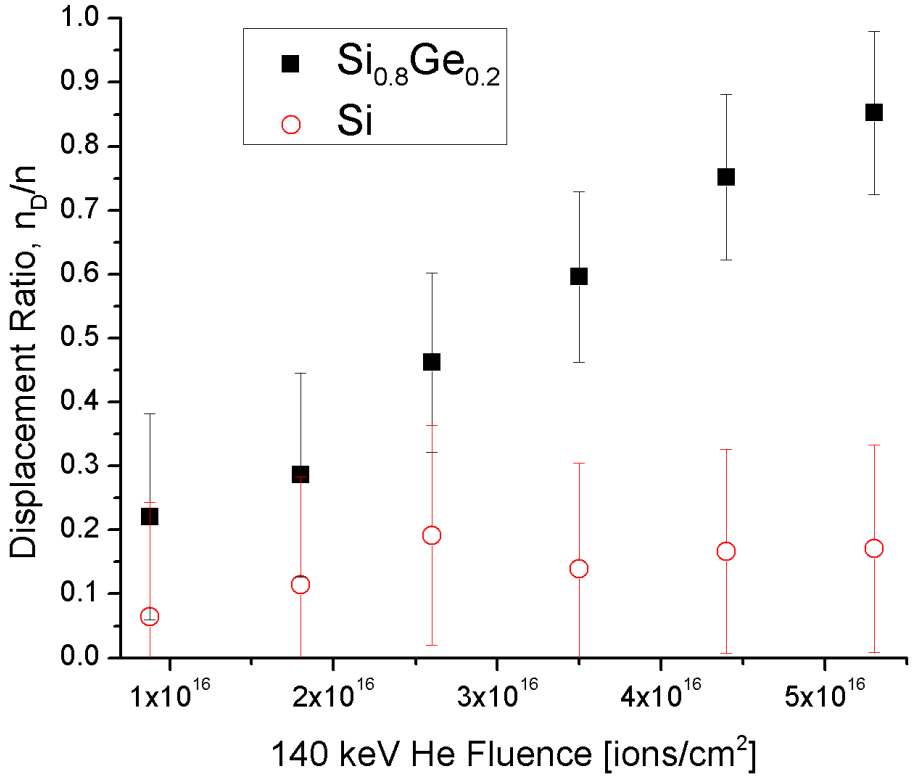

Fig. 24. The ratio of permanently displaced atoms n_D to total atoms n in $Si_{0.8}Ge_{0.2}$/Si and bulk Si irradiated by 140 keV He ions as calculated from RBS angular scans of $\langle 110 \rangle$ axis [24].

$$P_{I,V} \approx 4\pi r e^{-\frac{E}{kT}} C_I(t) C_V(t)(D_I + D_V). \tag{5.2}$$

For the case of bulk Si, we hypothesize that such a quasi-steady state point defect concentration has been acheived by the chosen irradiation conditions. The lack of dependence of displacement ratio on 140 keV He ion fluence of bulk Si in Figure 24 suggests this is true. No such saturation occurs in the strained SiGe layer irradiated by the chosen conditions, therefore

$$P_{I,V} \gg 4\pi r e^{-\frac{E}{kT}} C_I(t) C_V(t)(D_I + D_V). \tag{5.3}$$

For the stated assumptions, a defect recombination parameter must be changed by the presence of strain which causes decreased defect recombination. Reduced point defect diffusivities D_I and D_V or increased defect recombination energy E could cause this reduction in point defect dynamic recombination. It is also possible that the assumptions necessary for Equation 5.1 to be valid do not hold for a strained SiGe layer. It is possible that the structure of strained Si totally collapses under ion irradiation, or that extended point defects like dislocation loops are formed which would be trapping sinks for point defects, inhibiting point defect recombination. Relaxation of the strained layer would create dislocations, which would trap certain point defects, decreasing the amount of I-V recombination.

The next experiment will investigate the mechanism of permanent displacement creation in strained surface SiGe and bulk Si. The stability of strain will investigated later in this study as well. However, investigation of higher order defect formation and growth will not be investigated in this study.

Angular scans of the $\langle 100 \rangle$ and $\langle 111 \rangle$ axes after ion irradiation to $3.5 \times 10^{16} cm^{-2}$

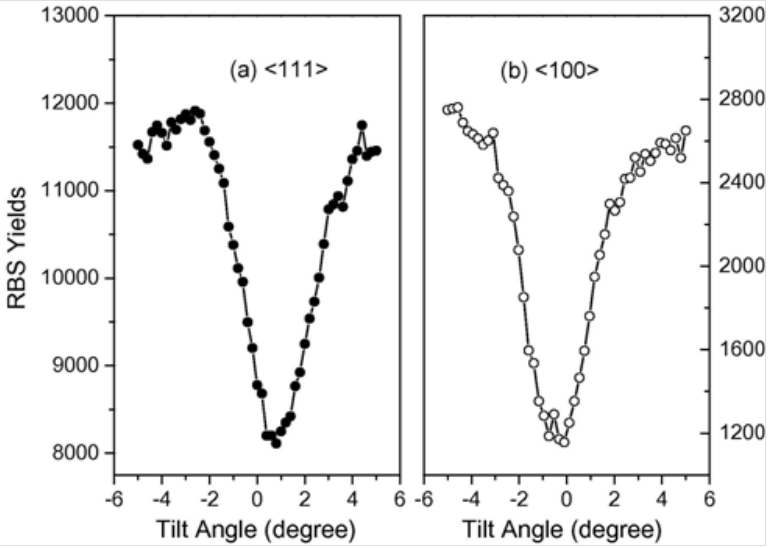

Fig. 25. RBS angular scans along the (a) ⟨111⟩ and (b) ⟨100⟩ axes of strained SiGe surface layer after 140 keV He ion irradiation to $3.5 \times 10^{16} cm^{-2}$.

with 140 keV He ions are performed to ensure that defect accumulation occurs isotropically. If, for example, point defect diffusivity is strongly dependent on axial direction, point defects could accumulate preferentially in a specific channel. These angular scans are shown in Figure 25.

C. Conclusions

The radiation response of $Si_{0.8}Ge_{0.2}$/Si differs greatly from that of bulk Si to light ion irradiation. Permanent displacement creation in strained $Si_{0.8}Ge_{0.2}$/Si is much more efficient than in unstrained, bulk Si. In bulk Si, displacement creation and dynamic recombination come into equilibrium beyond a certain ion fluence. No such saturation of permanent displacement creation was observed in strained $Si_{0.8}Ge_{0.2}$/Si. Angular scans along the three major axes of $Si_{0.8}Ge_{0.2}$/Si did not reveal a preferred configuration of point defects. The enhancement of radiation damage accumulation in $Si_{1-x}Ge_x$/Si should be considered in the fabrication and use of $Si_{1-x}Ge_x$/Si-based

devices.

Comparison of the unirradiated scan of $Si_{0.8}Ge_{0.2}$/Si in Figure 22 with the expected scans due to differing defect configurations in Figure 11 suggests that Si and Ge atoms near the surface of as-grown 50 nm $Si_{0.8}Ge_{0.2}$/Si have slight displacements from their lattice positions. The effect of this on displacement energy or defect mobility is not known, but this phenomenon could contribute to reduced point defect recombination.

The shape of the angular scans in Figure 25 suggest there is no preferred lattice location for point defects and interstitial defects are randomly distributed.

Though little specific information about defect creation or recombination can be obtained from this experiment, the response of bulk Si and strained SiGe differed greatly to identical implantation conditions with medium energy He ions. Compared to bulk Si, strained SiGe with a free surface is very sensitive to medium energy light ion irradiation.

CHAPTER VI

AMORPHIZATION MODEL OF BULK SI AND STRAINED SILICON-GERMANIUM

As discussed in Chapter V, accelerated defect accumulation in strained SiGe could be caused by a number of things. In this chapter, we seek to investigate the amorphization models of bulk Si and surface strained $Si_{0.8}Ge_{0.2}$ to determine if permanent damage creation differs due to presence of strain.

A. Damage Cascade Overlap and Amorphization

A damage cascade is the volume of a crystal along the path of an incoming ion that contains defects created by close-encounter nuclear collisions. The volume depends on ion species and energy, atomic mass of target atoms, temperature of the target and other factors.

For a heavy ion, $Z_{ion} > Z_{target}$, the damage cascade volume can be modeled as a right cylinder from the surface of the target to the end of range of the ion because the ion will not undergo large deflection from its incoming trajectory [25]. Primary knock-on atoms, or the recoiling target atom after a nuclear collision with an incoming ion, will be directed out from the path of the incoming heavy ion.

A light ion, $Z_{ion} < Z_{target}$, can undergo large deflections from incoming trajectory. When the light ion scatters, both it and the primary knock-on atom will likely scatter forward, creating the appearance of a branch in the damage cascade. This is shown in Figure 26.

The crystalline damage from one incoming ion is not sufficient to cause amorphization, or collapse of crystal structure, in bulk Si. Literature reports that for bulk Si irradiated with ions species from Li to Kr with energies from $20 - 180$ keV with

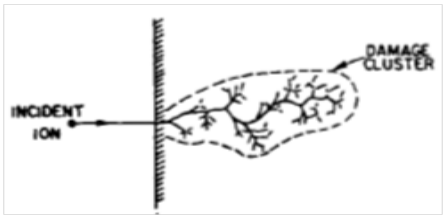

Fig. 26. A damage cascade volume created by an incident energetic ion [25].

the target temperature at 80 and 300 K, the increase in amorphous volume versus ion fluence indicates that permanent amorphization occurs by overlap of more than one damage cascade [26].

The process of formation of amorphous material is described by Gibbons in the equation [25]

$$\frac{A_A}{A_0} = 1 - \sum_{k=0}^{m-1} \frac{(A_i\phi)^k}{k!} exp(-A_i\phi) \tag{6.1}$$

where A_A/A_0 is the fraction of amorphized implantation area to total implantation area, A_i is the area amorphized by a single ion track in units of cm^2, $(m-1)$ is the number of overlaps required for amorphization and ϕ is the ion fluence in units of ions cm^{-2}. The value m is the number of ion damage cascades that must overlap to cause amorphization.

When amorphous fraction is plotted versus ion fluenc, increasing values of m will cause increase in the slope $dA_A/d\phi$. For implantation by single ions, plotting the amorphous fraction versus ion fluence and fitting the slope of that curve with Eq. 6.1 will determine the value of m. Amorphization versus ion fluence assuming different m values is shown in Figure 27.

Comparing the build-up with different values of m in Figure 27 with the experimental data in Figure 24, one would suspect that difference in the overlap number

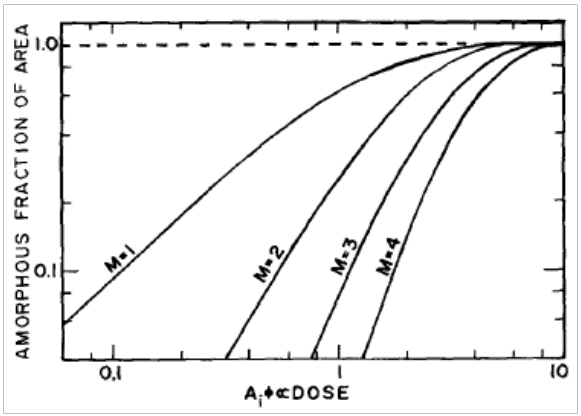

Fig. 27. The path to amorphization of bulk Si varies with the number of damage cascades that must overlap to cause amorphization [26]. The value m is the number of damage cascades that must overlap to cause collapse of crystal structure (amorphization).

of bulk Si and strained SiGe is the cause for accelerated defect accumulation in the strained SiGe layer under investigation. According to Dennis and Hale [26], in the case of bulk Si, $m \geq 2$. It seems likely that strain could cause a change in the way a material progresses to amorphization.

B. Cluster Ion Bombardment and Amorphization

Determining the overlap number by traditional ion implantation techniques suffers from the inherent difficulty that overlapping of damage cascades from single ions is statistical in nature. However, if cluster ions are implanted to a sufficiently low fluence so that clusters are unlikely to bombard the same point on the surface, crystalline damage as a function of cluster size will indicate the most favorable overlap number. Additionally, the energy per atom as well as atomic fluence ($atoms\ cm^{-2}$) incident on the sample should be held constant to apply cluster ion bombardment for the purpose of determining experimentally the value of m.

Shao *et al.* proposed a modification to Gibbons' overlap model to calculate per-

manent damage accumulation as function of cluster size for cluster ion bombardment [27]. The permanent damage volume fraction, proportional to the amorphous area fraction of Eq. 6.1, is described by

$$\frac{V_d}{V_0} = 1 - \sum_{k=0}^{m-1} \frac{(\delta n)^k}{k!} exp(-\delta n) \tag{6.2}$$

where the terms are identical to Eq. 6.1 except for $\delta = V_i/V_0$ is the ratio of individual cascade volume to total implanted volume [27]. Values for δ have been analytically calculated by Sigmund *et al.* as a function of the ratio of projectile mass to target mass [28].

The permanent displacement creation per cluster atom created by bombardment with cluster ions with n atoms per cluster is shown in Figure 28. For the direct amorphization model, $m = 1$, permanent damage creation is most efficient for single ion bombardment. For the overlap models, damage creation is most efficient for the case of $n = m$.

C. Experimental Procedure

Bulk n-type (100) orientation Si and 50 nm $Si_{0.8}Ge_{0.2}$/Si strained layer superlattice were irradiated with $n \times 12$ keV Ag_n cluster ions ($n = 1, 2, 3, 4$) to atomic fluences of 5×10^{13} *atoms* cm^{-2}. Cluster-bombarded samples were characterized by channeling Rutherford backscattering spectrometry with 300 keV He^{++} beam of the $\langle 100 \rangle$ (surface-normal) axis at Texas A&M University. The pressure in the target chamber is ¡5×10^{-8} torr by use of diffusion pump, cryogenic pump and liquid nitrogen cold trap in the chamber. A PIPS detector located at 170° backscattering angle cooled with liquid nitrogen with resolution estimated to be 14 keV is used to collect backscattered

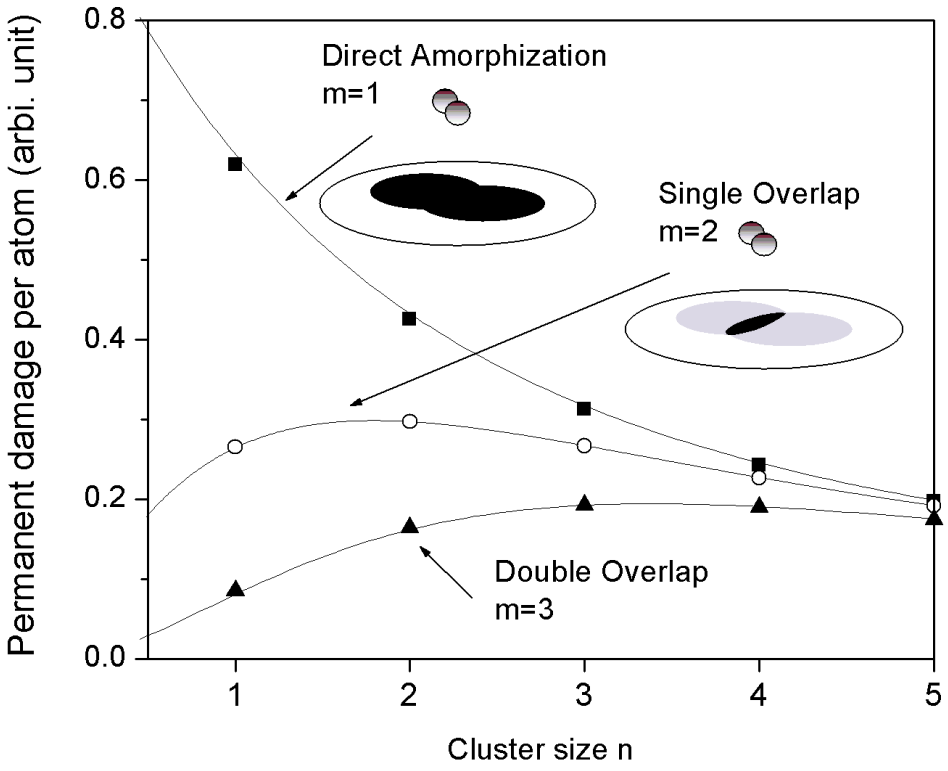

Fig. 28. The amount of permanent damage creation per atom due to cluster bombardment with n atoms per cluster [27].

He signal.

Channeling energy spectra are collected from each Ag implanted sample, as well as from unirradiated bulk Si and unirradiated 50 nm $Si_{0.8}Ge_{0.2}$/Si.

The permanent displacement ratio for cluster bombarded samples are plotted versus cluster size to determine the value of m, the number of damage cascades that overlap to cause amorphization.

D. Results and Discussion

Figure 29 shows five RBS channeling energy spectra collected on the $\langle 100 \rangle$ axis and one random energy spectrum. Four channeling spectra correspond to 50 nm $Si_{0.8}Ge_{0.2}$/Si implanted with Ag_n cluster ions where $n = 1, 2, 3, 4$, and one channeling spectra was taken from an as-grown 50 nm $Si_{0.8}Ge_{0.2}$/Si strained layer superlattice sample. The channeling spectra indicate displacements were created in the near-surface region at a depth less than 50 nm. The range of 12 keV Ag atoms is approximately 12 nm according to the Monte Carlo simulation code Stopping and Ranges of Ions in Matter (SRIM) [29].

Figure 30 shows five RBS channeling energy spectra collected by analysis of the $\langle 100 \rangle$ axis and one random energy spectrum. Four channeling energy spectra are from bulk Si implanted with Ag_n cluster ions where $n = 1, 2, 3, 4$, and one channeling spectra was taken from unirradiated bulk Si. As in Figure 29, displacement concentration is high in the near-surface region. Visual inspection of channeling spectra of the cluster implanted bulk Si samples in Figure 30 indicates that the fewest displacements are created by irradiation by Ag_1 ions.

The ratio of permanently displaced Si or Ge atoms to total number of Si or Ge atoms for the peak damage regions in the Si and Ge backscattering signals in $Si_{0.8}Ge_{0.2}$

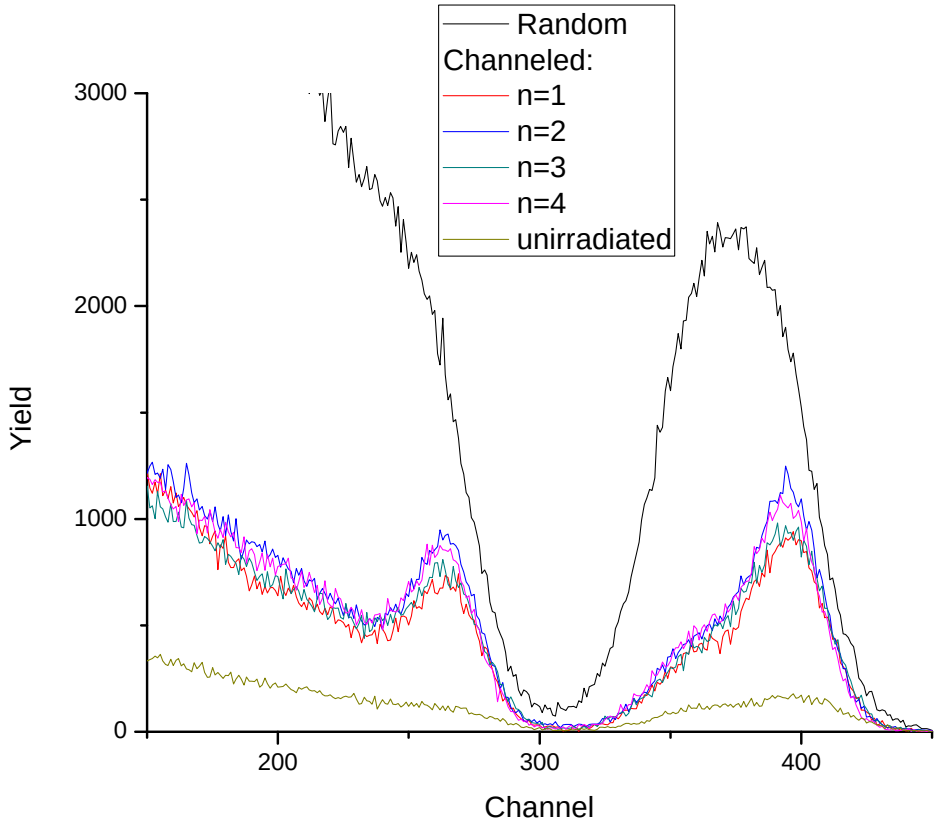

Fig. 29. RBS channeling spectra of the $\langle 100 \rangle$ axis collected using 300 keV He of unirradiated and Ag_n $(n = 1 - 4)$ cluster implanted 50 nm $Si_{0.8}Ge_{0.2}/Si$ samples as well as a random spectrum of 50 nm $Si_{0.8}Ge_{0.2}/Si$.

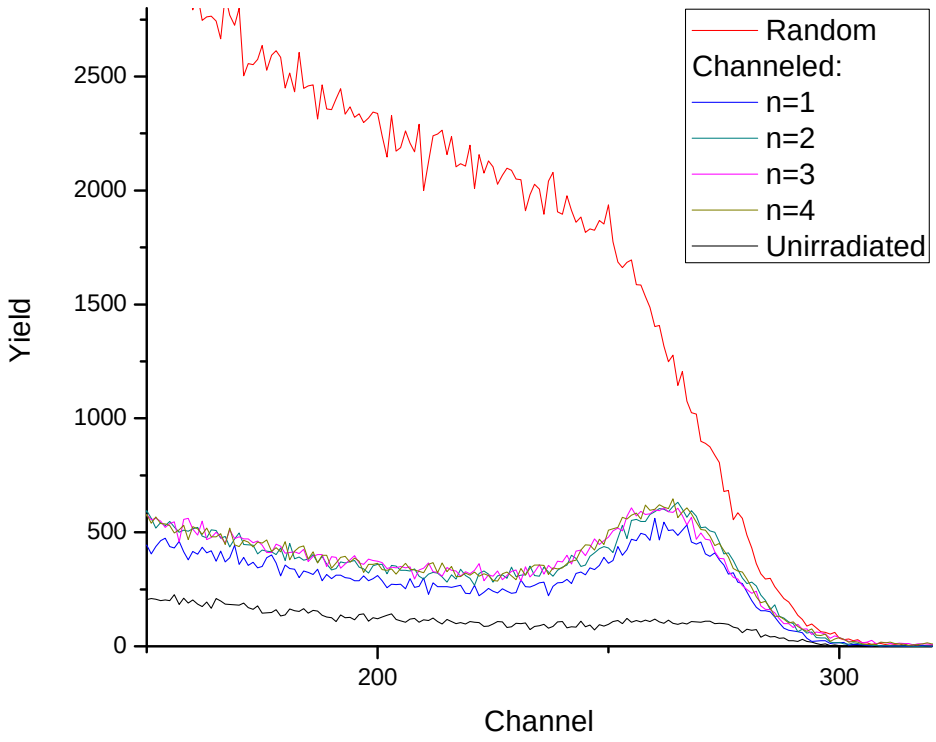

Fig. 30. RBS channeling spectra of the $\langle 100 \rangle$ axis collected using 300 keV He of unirradiated and Ag_n $(n = 1 - 4)$ cluster implanted bulk Si as well as a random bulk Si spectrum.

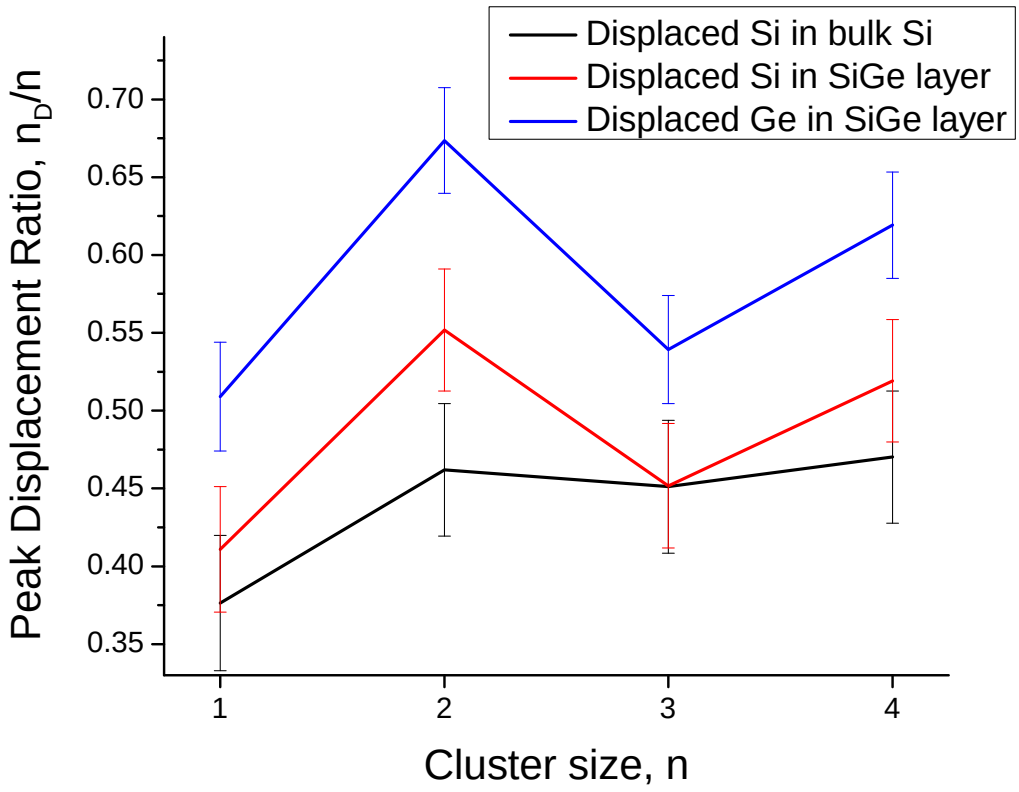

Fig. 31. Peak Si and Ge displacement ratios n_D/n in $Si_{0.8}Ge_{0.2}$ and bulk Si caused 12 keV/atom Ag_n ($n = 1-4$ atoms) cluster ion implantation to fluence 5×10^{13} atoms cm^{-2}.

will be compared to that of the peak damage region in bulk Si by application of Eq. 5.1. This data can be found in Figure 31 and Table I. Counts from channels $256-270$ were integrated to calculate Si displacements in bulk Si and strained $Si_{0.8}Ge_{0.2}$, and counts from channels $386-400$ were integrated to calculate Ge displacements in strained $Si_{0.8}Ge_{0.2}$.

Table I. Peak Si and Ge displacement ratios in strained $Si_{0.8}Ge_{0.2}$ and bulk Si samples created by 12 keV/atom Ag_n ($n = 1 - 4$ atoms) cluster ion implantation to fluence 5×10^{13} atoms cm^{-2}.

Atoms per Ag cluster, n	Si in bulk Si	Si in $Si_{0.8}Ge_{0.2}$	Ge in $Si_{0.8}Ge_{0.2}$
1	0.376 ± 0.043	0.411 ± 0.040	0.509 ± 0.035
2	0.462 ± 0.043	0.552 ± 0.039	0.674 ± 0.034
3	0.451 ± 0.043	0.452 ± 0.040	0.539 ± 0.035
4	0.470 ± 0.042	0.519 ± 0.039	0.619 ± 0.034

E. Conclusions

Irradiation by Ag_2 cluster ions creates more permanent Si and Ge displacements in strained $Si_{0.8}Ge_{0.2}$ and bulk Si than irradiation by Ag_1 monomer ions. Bulk Si follows a damage cascade overlap model to become amorphous, in agreement with the findings of Dennis and Hale [26] and Shao *et al.* [27]. Strained $Si_{0.8}Ge_{0.2}$ follows an overlap model in the progression from crystalline to amorphous. For strained $Si_{0.8}Ge_{0.2}$ and bulk Si implanted by 12 keV Ag ions to low fluence, $m > 1$. The precise value of m, the number of cascades that must overlap to create amorphization, can not be definitively concluded.

The trend in Si and Ge displacements for $n = 3$ and $n = 4$ can not be explained. As an aside, this is a challenging experiment, and contamination of the Ag_2 beam by Ag_4^{2+} is possible because the beam was mass-analyzed by mass-to-charge ratio.

Additionally, the increase in displacements in strained $Si_{0.8}Ge_{0.2}$ supports the original hypothesis that efficiency of point defect recombination is reduced by strain.

The difference in the response of strained SiGe and Si is not based on the reaction to energy deposition by an incoming energetic ion; strain does not change the progression of amorphization. The difference in radiation response in strained SiGe

and bulk Si must be in the recombination and annihilation of point defects.

CHAPTER VII

MEASURING STRAIN AND POINT DEFECT CONCENTRATION IN SURFACE AND BURIED STRAINED SILICON-GERMANIUM LAYERS BY TWO-DIMENSIONAL BACKSCATTERING YIELD MAPPING

Point defect accumulation and strain can be determined by comparing ⟨110⟩-axis backscattering yield maps of strained SiGe and bulk Si layers. Mapping of pure Si layers in $Si_{0.8}Ge_{0.2}$/Si and Si/$Si_{0.8}Ge_{0.2}$/Si layers will be performed to verify these layers are identical to bulk Si. Surface layers, both pure Si and $Si_{0.8}Ge_{0.2}$, are 50 nm thick, and buried $Si_{0.8}Ge_{0.2}$ layer is 60 nm thick.

The accumulation of point defects created by repeated analysis with 2 MeV He of buried and surface strained $Si_{0.8}Ge_{0.2}$ layers indicates the free surface has a strong effect on dynamic defect recombination. The effect of repeated analysis with 2 MeV He on strain was not significant. Analysis of surface and buried strained SiGe layers implanted with 140 keV He ions indicates that the free surface has an effect on strain stability and on defect accumulation.

Finally, in an effort to understand this method of strain measurement, the effect of depth of strained layer on strain measurement, as shown in Figure 19, will be investigated. Strain in an as-grown, 5 nm thick $Si_{0.8}Ge_{0.2}$ layer with a 190 nm thick pure Si top layer will be measured. Our conclusion supports that of Chu et al. in [22], that underestimation of strain increases with depth of the strained layer.

A. Experimental Procedure

Three strained layer superlattice samples will be investigated in this experiment. Samples grown on (100) orientation bulk Si substrates by molecular beam epitaxy at 650 C consisting of 50 nm $Si_{0.8}Ge_{0.2}$/Si and 50 nm Si/60 nm $Si_{0.8}Ge_{0.2}$/Si will be

analyzed to determine strain and point defect accumulation caused by 140 keV or 2 MeV He ion irradiation. Surface and buried strained layer samples will be implanted with 140 keV He ions to fluences of 1 and 5×10^{16} ions cm^{-2}. Analysis with 2 MeV He ions will be repeated so that the analyzing beam will cause irradiation damage, with maximum fluence of 2 MeV He estimated to be 3.2×10^{17} ions cm^{-2}. An as-grown, unirradiated 190 nm Si/5 nm $Si_{0.8}Ge_{0.2}$/Si sample will be analyzed to determine strain. No sample can truly be called "unirradiated" following the analysis performed because each map requires approximately three hours of continuous analysis with 2 MeV He ion beam. The integrated charge for each map is well known, but the beam spot size must be estimated, leading to uncertainty in the absolute value of 2 MeV He ion fluence. The estimate of the beam spot size area is assumed to be constant, so comparison between different samples irradiated with certain fluence of 2 MeV He ions is valid. Additionally, 50 nm Si/60 nm $Si_{0.8}Ge_{0.2}$/Si samples irradiated with 140 keV He ions to fluences of 1 and 5×10^{16} ions cm^{-2} are analyzed with 2 MeV He ions to determine strain and defect concentration.

Buried and surface strained SiGe layers will be analyzed by the channeling Rutherford backscattering spectrometry based technique referred to as backscattering yield mapping, described in Section 5. Backscattering yields from individual layers in the strained layer superlattice samples will be collected about the $\langle 110 \rangle$ axis and plotted as a function of angle along the [100] plane (ordinate axis in maps) and [110] plane (abscissa), as measured between the surface normal $\langle 100 \rangle$ axis and the incident ion beam direction.

Samples are analyzed by 2 MeV He in a multi-purpose analysis chamber attached to the 1.7 MV Tandetron at the Texas Center for Superconductivity at the University of Houston. Collaborators at TCS-UH are Dharshana Wijesundera, a Ph.D student, and Xuemei Wang, who work in the Ion Beam Lab research group headed

by Dr. Wei-Kan Chu. A PIPS detector at 165° backscattering angle from incident ion beam direction collects quantity of backscattered He particles, which are then routed through pre-amplifier, amplifier, then single channel analyzer before counts are discretized and plotted as a function of particle energy by mutli-channel analyzer software in a desktop computer. It is not common for the backscattering signal to pass through a single channel analyzer before a multi-channel analyzer, but the purpose for this sequence will be explained shortly. For collection of energy spectra, the single channel analyzer lower level discriminator is set to its minimum value and the upper level discriminator is set to its maximum value, meaning that the single channel analyzer allows all data to pass to the multi-channel analyzer. For angular scanning, the single channel analyzer is set to only allow counts from a chosen energy window, which is equivalent to a selected depth window, to pass to the multi-channel analyzer. Examples of the energy regions selected for mapping of different layers in strained layer superlattices is shown in Figure 32. For mapping, the multi-channel analyzer is bypassed; counts from the single channel analyzer are integrated and recorded with the polar position of the sample in Microsoft Excel by proprietary software written by Dharshana Wijesundera.

Upon loading the sample, the $\langle 100 \rangle$ axial channel is found by collecting a series of energy spectra and angular scans. First, an energy spectrum with the sample in any alignment is collected in order to determine the energy interval for angular scanning. The energy interval corresponding to a constituent of the sample's surface layer is selected, and angular scans forming a box shape are collected. The sample is tilted 3° from the incident ion beam in all four directions and angular scans are performed across an interval of 6°. For instance, the first angular scan performed would start at the polar position -3° horizontal tilt, or counter-clockwise rotation from top-view, and -3° vertical tilt, measured from the incident ion beam direction with respect to the

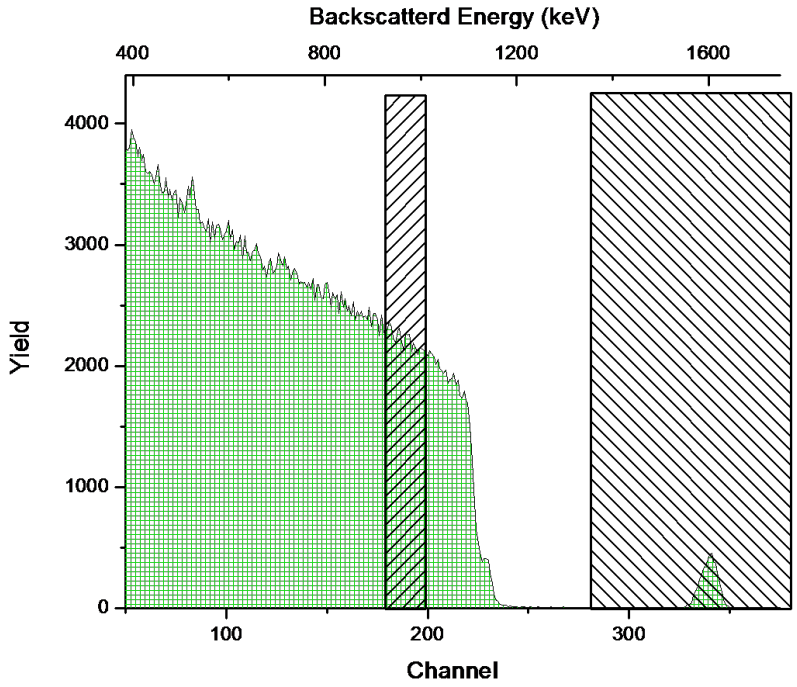

Fig. 32. Random RBS spectrum from 50 nm $Si_{0.8}Ge_{0.2}$/Si showing the method for choosing the energy window for two-dimensional backscattering yield mapping the $\langle 110 \rangle$ axis

outward surface normal. Horizontal tilt angle is fixed, and the sample is rotated from -3° to +3°, with counts resulting from a fixed integrated charge of He ions recorded at small angular intervals, usually 0.1°. Four such angular scans are collected, and the minima of counts of each are plotted. The global minima of these scans correspond to the tilt angles of orthogonal [100] planes parallel to the surface plane. Local minima correspond to higher-index planes. The intersection point in the polar plot of all minima from these four scans corresponds to the ⟨100⟩ axial channel. This method is referred to as the "box" method because, in polar coordinates, a box is traced by the four angular scans. The goal of this method is to align the surface normal direction with the incident ion beam direction.

Following sample alignment with the ion beam, the sample is tilted -45° (counter-clockwise when viewed from the top of the sample) and the box method is repeated to find the ⟨110⟩ axial channel. However, when the sample surface normal is tilted more than a few degrees away from the incident ion beam direction, angular scans with one tilt angle fixed are distorted. In order to find an off-normal axial channel using the "box" method, this limitation is overcome by repeating the procedure. However, the goal of this experiment is to collect many angular scans which, when combined, will create a backscattering probability surface, which is useless if the polar coordinates lack physical meaning [23]. If, for example, the vertical tilt angle is fixed at +1°, the polar path the beam traces for this angular scan is not parallel to the path of an angular scan with a different fixed vertical tilt angle. Polar coordinates must be transformed to ensure angular scans' stereographic projections are parallel. The sample's polar coordinates, the horizontal and vertical tilt settings, must be multiplied by a transformation matrix in order to determine the true polar projection of the beam on the sample with respect to the original axis of beam alignment. This coordinate tranformation can be applied before or after data collection, but

application after data collection will lead to asymmetric mapping intervals. The coordinate transformation is performed before data collection in this experiment so that mapping axes are perpendicular. After ensuring that angular scan projections are parallel, mapping the ⟨110⟩ axial channel is performed. The tilt angle step in the [100] planar direction, the ordinate axis, is set to 0.1°. High precision is necessary because strain is expected to shift in this direction. The tilt angle step in the [110] planar direction, the abscissa, vary between 0.1° and 0.2° depending on the details of each map: a coarser step size is used on a large map so that the time, and, consequently, 2 MeV He ion fluence, required to collect the map is reasonable. Alternately, analysis time and fluence can be reduced in samples that have high backscattering yield by decreasing the integrated charge, or analyzing beam fluence, at each angular position.

Maps in the following section show a yield value plotted as a function of angular position. The number of counts at each angular position is normalized by the average value of counts at every angular position to obtain a normalized yield value.

B. Results and Discussion

Figure 33 shows backscattering yield maps from Ge atoms in the surface SiGe layer and Si atoms in the buried, bulk Si layer in as-grown $Si_{0.8}Ge_{0.2}$/Si sample. The minimum yields for maps in Figure 33 (b), (c) and (d) are 10%, 18% and 25%, respectively. As in Figure 24, defects accumulate linearly with increasing ion fluence. The magnitude of defect accumulation due to irradiation by 2 MeV He ion irradiation will be less than that by 140 keV He ion irradiation, but the trend is confirmed for high energy light ions. The location of the ⟨110⟩ axis appears constant with high energy light ion irradiation, and comparison of the angular position of minimum yield in maps (b)-(d) with that of (a) gives the value of $\Delta\theta$. For maps (b), (c) and (d) the

values for $\Delta\theta$ are 0.28°, 0.30° and 0.23°, respectively. Error is estimated to be half of the angular step, or 0.05 °. The meaured strains in maps in Figure 33 (b)-(d) are 0.98%, 1.05% and 0.81%, respectively, according to Eq. 3.1. Additionally, as predicted in Figure 18 from [22], the interface between strained and unstrained layers makes the ⟨110⟩ axis in buried bulk Si appear asymmetric. Significant asymmetry in the axial channel is characteristic of buried layers in this study; whether the buried layer is strained or unstrained has no effect.

Figure 34 shows the same experiment as Figure 33 performed on as-grown 50 nm Si/60 nm $Si_{0.8}Ge_{0.2}$/Si. The surface Si map indicates that the strained layer has no effect on its properties. Minimum yield does not increase with increasing analyzing beam fluence in the buried SiGe layer. By comparing the position of minimum yield in map (a) in Figure 33 with those of maps (c)-(e), the value of $\Delta\theta$ will be determined. For maps (c), (d) and (e) of 33, the values of $\Delta\theta$ are 0.25°, 0.27° and 0.27°, respectively. According to Eq. 3.1, the measured strains in the buried $Si_{0.8}Ge_{0.2}$ layer in maps (c), (d) and (e) are 0.88%, 0.95% and 0.95%, respectively. The angular offset, and therefore strain, in the ⟨110⟩ axis of differing Si and Ge layers in Figure 34 is similar to that of Figure 33. The minimum yield in the buried strained $Si_{0.8}Ge_{0.2}$ layer is stable with increasing 2 MeV He ion fluence, with the minimum yield increasing by around 1% due to 2 MeV He ion irradiation, and the location of the ⟨110⟩ axis in the buried strained $Si_{0.8}Ge_{0.2}$ layer does not shift considerably with increasing 2 MeV He ion fluence.

Maps from the top two layers of Figures 33 and 34 are plotted in Figure 35 to qualitatively judge the shift in the location of the ⟨110⟩ axis. Both surface and buried strained SiGe layers show no shift in strain due to high fluence 2 MeV He ion irradiation because the axial location does not change. We can be confident that collection of 2-D backscattering yield maps does not measurably alter strain.

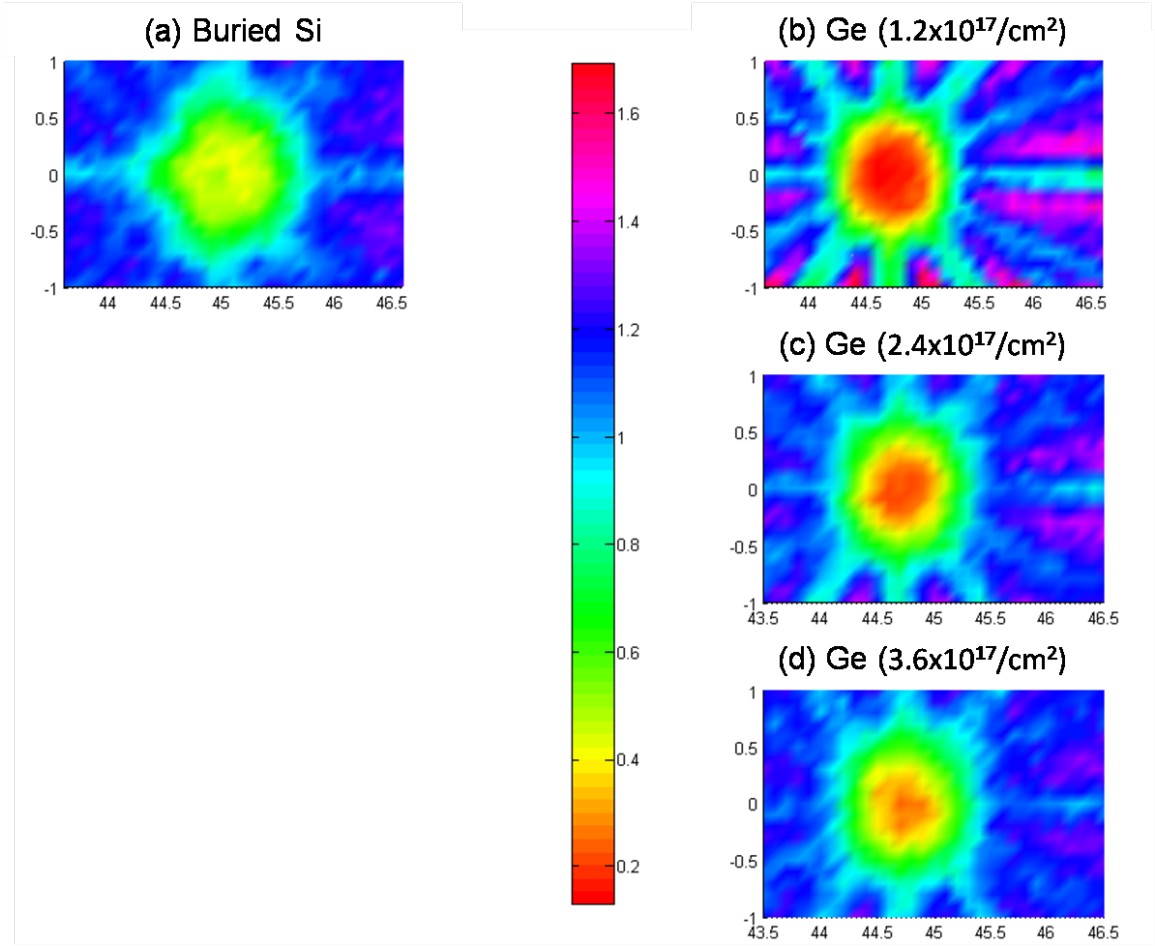

Fig. 33. Two-dimensional backscattering yield maps about the ⟨110⟩ axis of 50 nm $Si_{0.8}Ge_{0.2}$/Si. (a) shows the map of buried, unstrained Si, (b) shows the first map of Ge which required estimated fluence of 1.2×10^{17} cm^{-2} 2 MeV He ions to collect, (c) and (d) show the same map as (b) collected sequentially, where total 2 MeV He ion fluence after collection was 2.4 and 3.6×10^{17} cm^{-2}, respectively. Minimum yield increases from approximately 10% to 25% from (b) to (d).

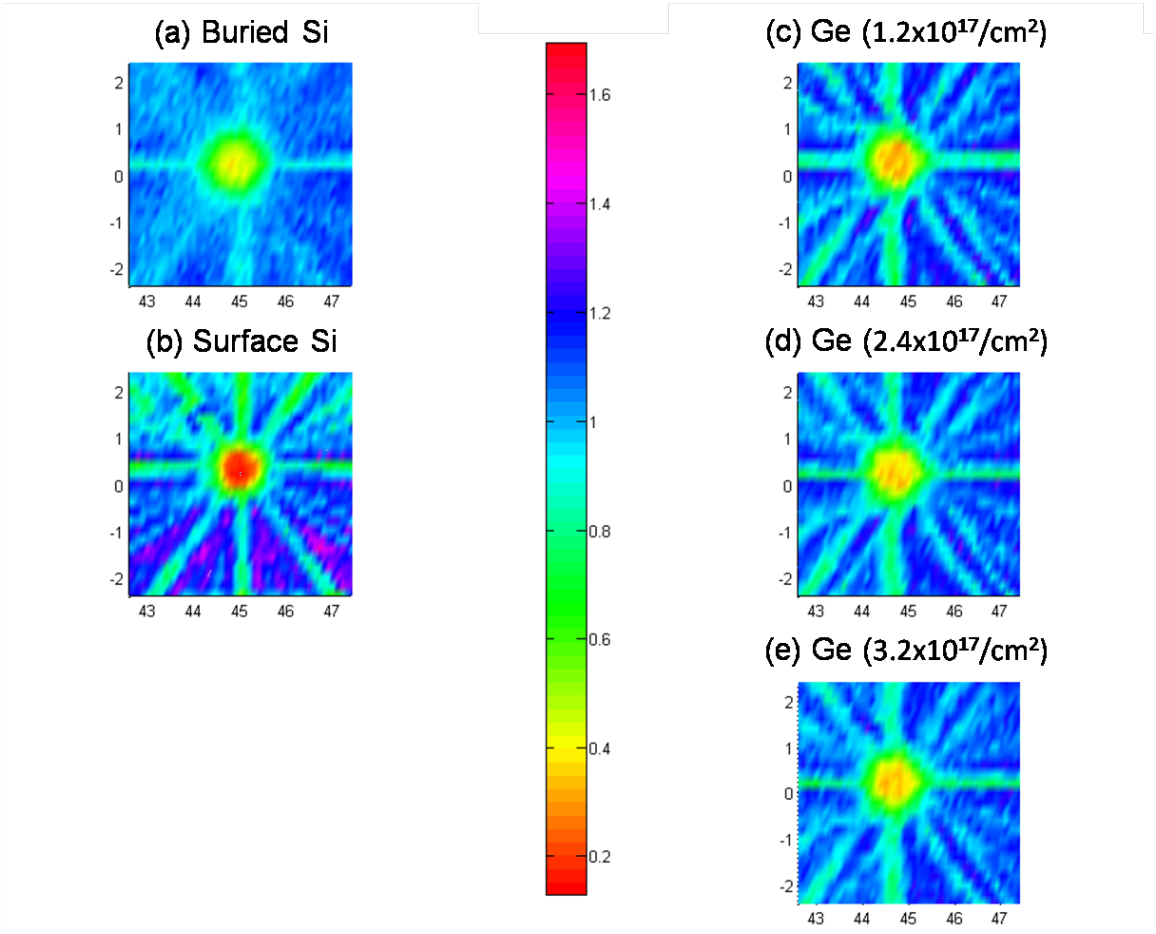

Fig. 34. Two-dimensional backscattering yield maps about the ⟨110⟩ axis of 50 nm Si/60 nm $Si_{0.8}Ge_{0.2}$/Si, with (a) buried, unstrained Si, (b) surface, unstrained Si, (c) shows the first map of Ge which required estimated fluence of 1.2×10^{17} cm^{-2} 2 MeV He ions to collect, (d) and (e) show the same map as (c) collected sequentially, where total 2 MeV He ion fluence after collection was 2.4 and 3.6×10^{17} cm^{-2}, respectively. Minimum yields for (c), (d) and (e) are 31%, 32% and 32%, respectively.

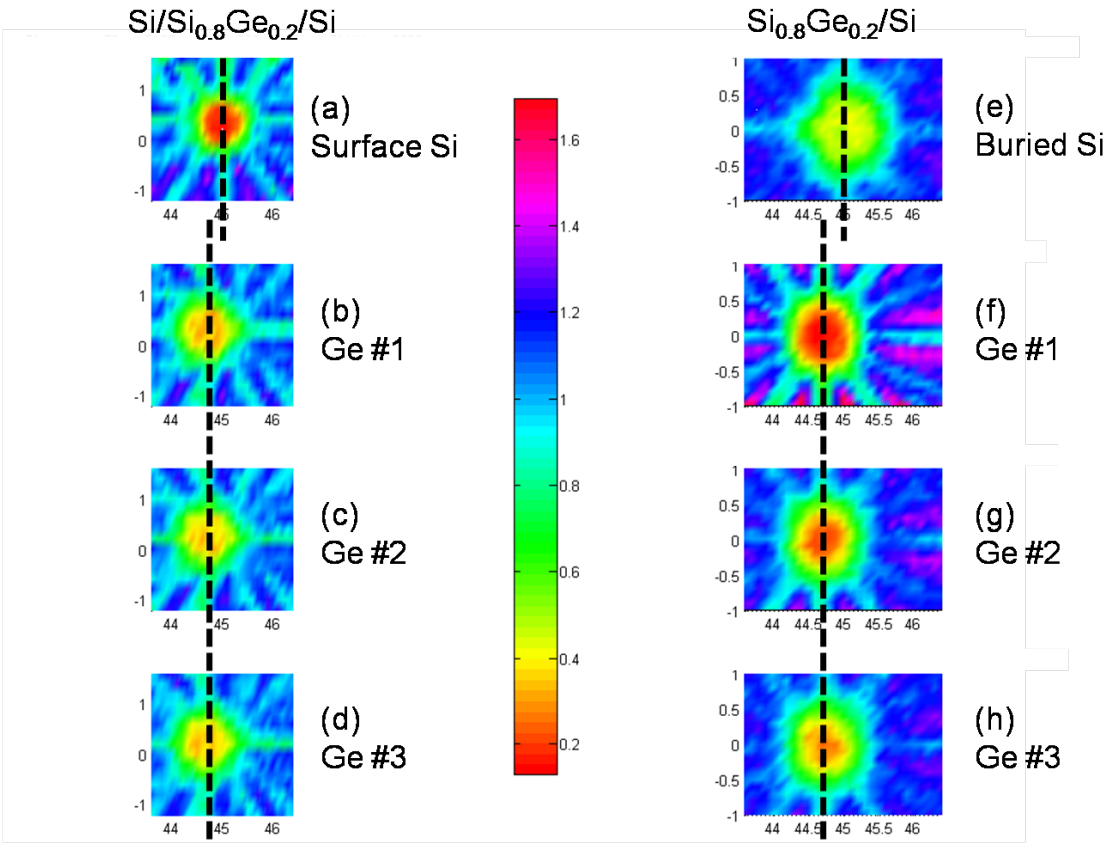

Fig. 35. Two-dimensional backscattering yield maps about the ⟨110⟩ axis of 50 nm Si/60 nm $Si_{0.8}Ge_{0.2}$/Si, (a)-(d), and of 50 nm $Si_{0.8}Ge_{0.2}$/Si, (e)-(h). These maps are re-plotted from Figures 33 (b)-(d) and 34 (a)-(d) in order to show that there is no shift in the position of the ⟨110⟩ axis after repeated analysis with 2 MeV He beam.

Maps of the as-grown samples of both 50 nm Si/60 nm $Si_{0.8}Ge_{0.2}$/Si and of 50 nm $Si_{0.8}Ge_{0.2}$/Si have an unexpected shape. The buried layer in each sample appears to be asymmetric. In order to better understand this, the value of Lindhard's critical angle was calculated for 2 MeV He along the $\langle 110 \rangle$ axis and the maps in Figures 34 and 33 are re-plotted showing yield values $\leq 50\%$. Figures 36 and 37 show the shape of the $\langle 110 \rangle$ axial channel in different layers. It is clear that asymmetry extends into the low-yield, channeled portion of the energy spectrum. The concept underlying Lindhard's critical angle is that channeling is caused by many parallel strings of atoms with a uniform potential field which steers energetic particles by electronic collisions [17]. The axial channel formed by these conditions can be quantified and compared by the critical angle. In this treatment of the axial channel, symmetry about the center of the channel is assumed. Clearly, symmetry can not be assumed in the case of SiGe strained layer superlattices.

The unirradiated surface layers, Figure 36.B and Figure 37.B(1), are the most symmetric in their respective samples. Asymmetry in the pure Si surface layer in Figure 36.B is minimal and could be caused by statistical fluctuation. The map of Ge in $Si_{0.8}Ge_{0.2}$/Si shown in Figure 37.B(1) appears to be elliptic. As analyzing beam fluence increases in Figure 37.B(2)-(3), the channel shrinks in size, as is to be expected when defects are created, but the elliptic shape persists. Table II contains the dimensions of the channels shown in Figures 36 and 37. These values are the maximum angular interval of the horizontal and vertical directions in the maps plotted, which correspond to the directions parallel to the [100] and [110] planes. In highly asymmetric maps, these values probably have no physical meaning, but are tabulated here for the sake of comparison.

Buried strained layer samples, 50 nm Si/60 nm $Si_{0.8}Ge_{0.2}$/Si, were implanted with 140 keV He ions to fluences of 1×10^{16} cm^{-2} and 5×10^{16} cm^{-2} and the $\langle 110 \rangle$ axis was

Table II. Experimentally determined half-angles, $\psi_{1/2}$, from 50 nm $Si_{0.8}Ge_{0.2}$/Si and 50 nm Si/60 nm $Si_{0.8}Ge_{0.2}$/Si samples measured by 2 MeV He RBS. The data is extracted from Figures 36 and 37. The error of each half-angle value is $\pm 0.5°$.

$Si_{0.8}Ge_{0.2}$/Si	Signal	Run	$2\psi_{1/2}$ (horizontal)	$2\psi_{1/2}$ (vertical)
	Ge	1	0.85°	1.05°
		2	0.75°	1.0°
		3	0.75°	0.90°
	Buried Si	4	$0.7 - 0.75°$	0.6,0.8°
Si/$Si_{0.8}Ge_{0.2}$/Si				
	Surface Si	1	0.90°	0.95°
	Ge	2	0.95°	1.05°
		3	0.95°	1.0°
		4	0.95°	1.0°
	Buried Si	5	0.75°	0.75°

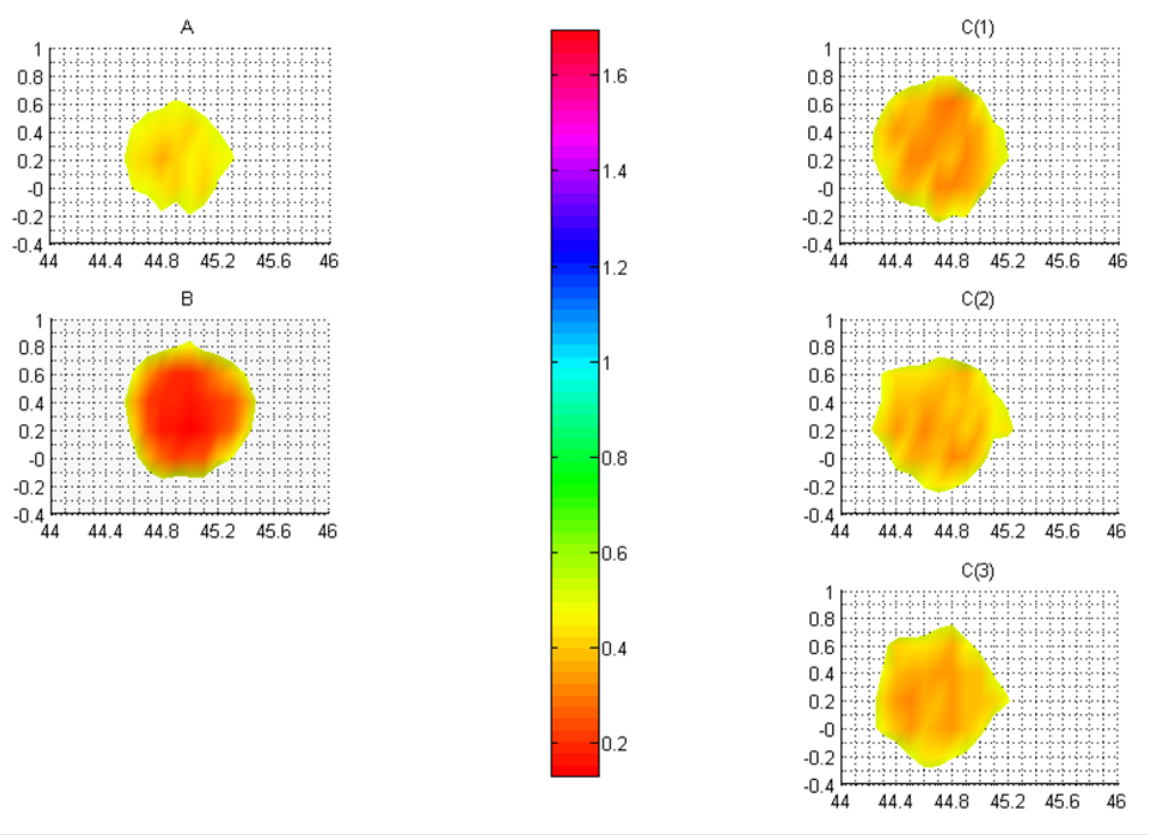

Fig. 36. Two-dimensional backscattering yield maps of layers in 50 nm $Si_{0.8}Ge_{0.2}$/Si, from Figure 34, showing the ⟨110⟩ axial channel. Yields of 50% or less are plotted. The shape of the channel changes in each layer. Map A is buried Si and maps B(1)-(3) are Ge in $Si_{0.8}Ge_{0.2}$ surface layer implanted to fluences of approximately 1.2, 2.4 and 3.6×10^{17} cm^{-2}, respectively, with 2 MeV He analyzing beam.

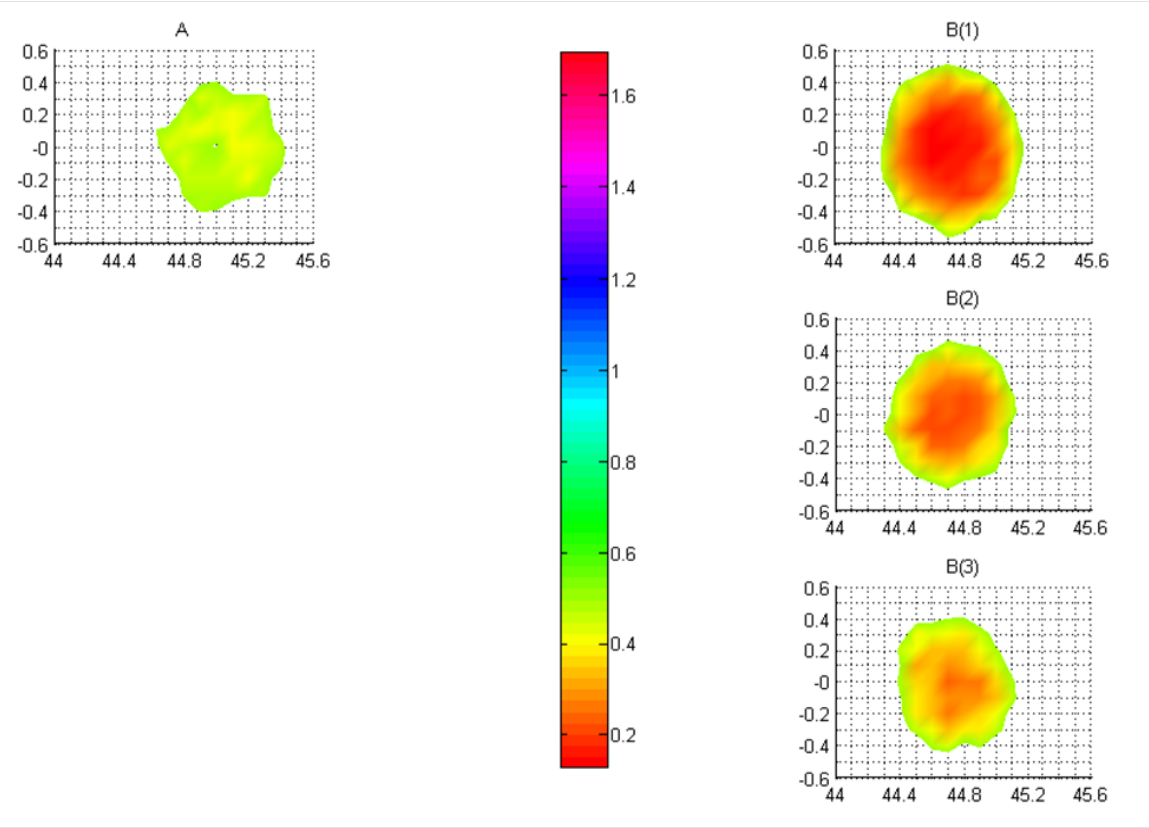

Fig. 37. Two-dimensional backscattering yield maps of layers in 50 nm Si/$Si_{0.8}Ge_{0.2}$/Si, from Figure 33, showing the ⟨110⟩ axial channel. Yields of 50% or less are plotted. The shape of the channel changes in each layer. Map A is buried Si, map B is surface Si and maps C(1)-(3) are Ge in $Si_{0.8}Ge_{0.2}$ buried layer implanted to fluences of approximately 1.2, 2.4 and 3.2×10^{17} cm^{-2}, respectively, with 2 MeV He analyzing beam.

analyzed by the method of 2-D backscattering yield mapping. Backscattering yield maps of the surface Si layer, Ge in the SiGe layer, and buried Si are shown in Figure 38 for both 140 keV He irradiation conditions. Unfortunately, it is hard to quantify strain in the 1×10^{16} cm^{-2} 140 keV He implanted sample because we did not collect a map from the surface Si layer due to time constraints. However, strain is confirmed in the 5×10^{16} cm^{-2} 140 keV He irradiated sample. Comparing the position of minimum yield the surface Si and buried SiGe layers gives $\Delta\theta = -0.27°$. According to Eq. 3.1, the tensile out-of-plane strain in the 5×10^{16} cm^{-2} 140 keV He ion implanted 60 nm $Si_{0.8}Ge_{0.2}$ buried layer is 0.95%. This value for strain is consistent with those obtained from Figure 34.

Finally, the question of the depth limitation of the technique of backscattering yield mapping when applied to measurement of out-of-plane strain will be briefly investigated. A 190 nm Si/5 nm $Si_{0.8}Ge_{0.2}$/Si strained layer superlattice sample previously confirmed by Shao *et al.* to be fully strained will be investigated by backscattering yield mapping of the $\langle 110 \rangle$ axis [30]. Figure 39 shows strain in this sample as measured by X-ray diffraction, and Figure 40 shows backscattering yield maps of surface Si layer and Ge in the buried SiGe layer about the $\langle 110 \rangle$ axis. There is no significant difference in the position of the $\langle 110 \rangle$ axis between the two layers. The sensitivity of this technique is inversely proportional to the thickness of the surface layer. For tensile out-of-plane strain due to $Si_{0.8}Ge_{0.2}$, a surface layer thickness of 190 nm causes the technique of backscattering yield mapping of the $\langle 110 \rangle$ axis with 2 MeV He to measure zero strain in a layer where strain has been confirmed.

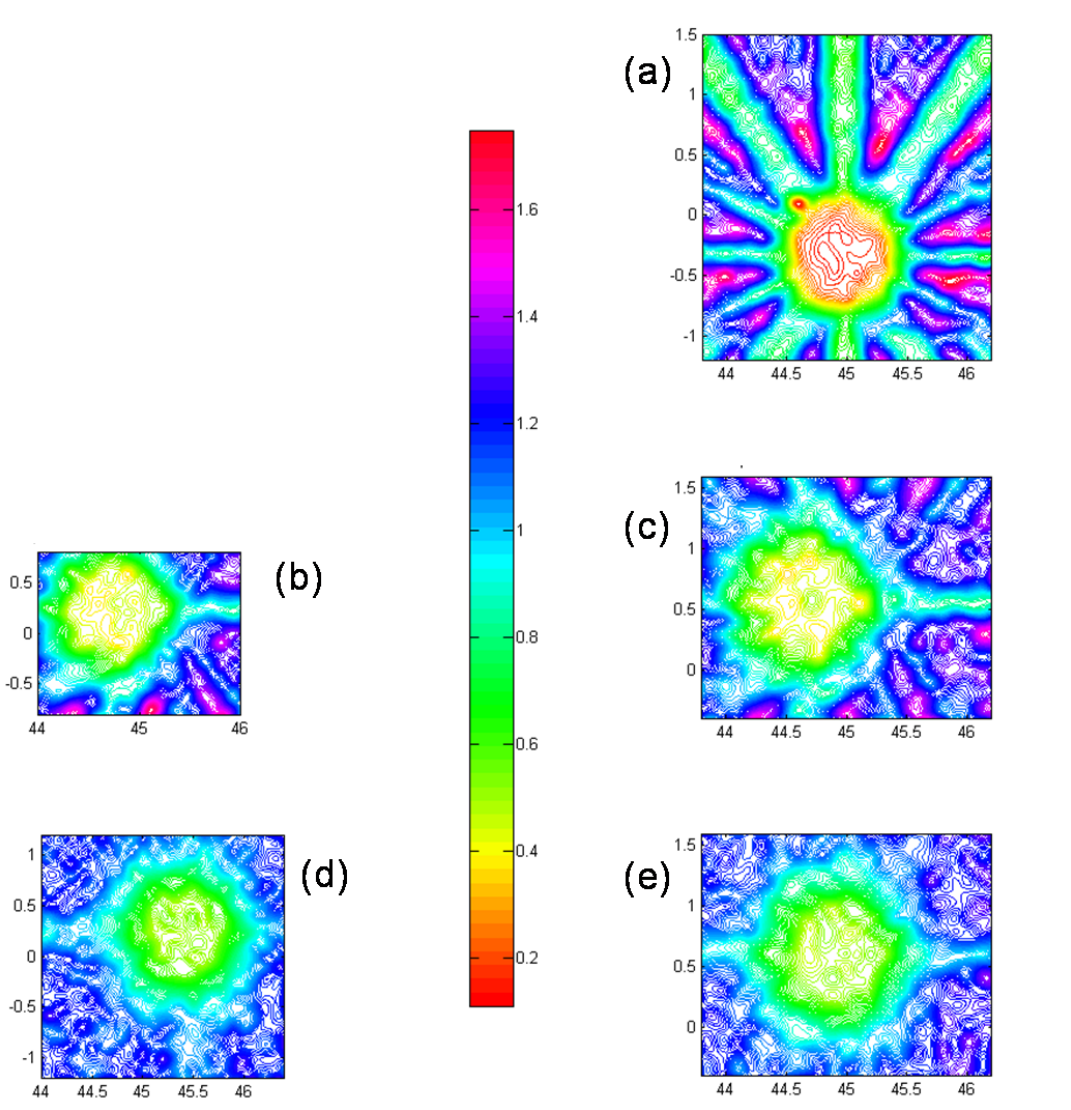

Fig. 38. Two-dimensional backscattering yield maps about the ⟨110⟩ axis of 50 nm Si/60 nm $Si_{0.8}Ge_{0.2}$/Si implanted with 140 keV He ions. Maps (a), (c) and (e) are implanted with 5×10^{16} cm^{-2} 140 keV He ions, and maps (b) and (d) are implanted with 1×10^{16} cm^{-2} 140 keV He ions. Map (a) is the surface Si layer, maps (b) and (c) are Ge in the buried $Si_{0.8}Ge_{0.2}$ layer, and maps (d) and (e) are from buried Si. The minimum yields in maps (a)-(e) are 5%, 36%, 36%, 45% and 44%, respectively. The offset in the position of minimum yield between maps (a) and (c) is 0.27°, corresponding to strain of 0.95%, according to Eq. 3.1. Implantation with 5×10^{16} cm^{-2} 140 keV He does not change strain in 50 nm Si/60 nm $Si_{0.8}Ge_{0.2}$/Si as measured by RBS.

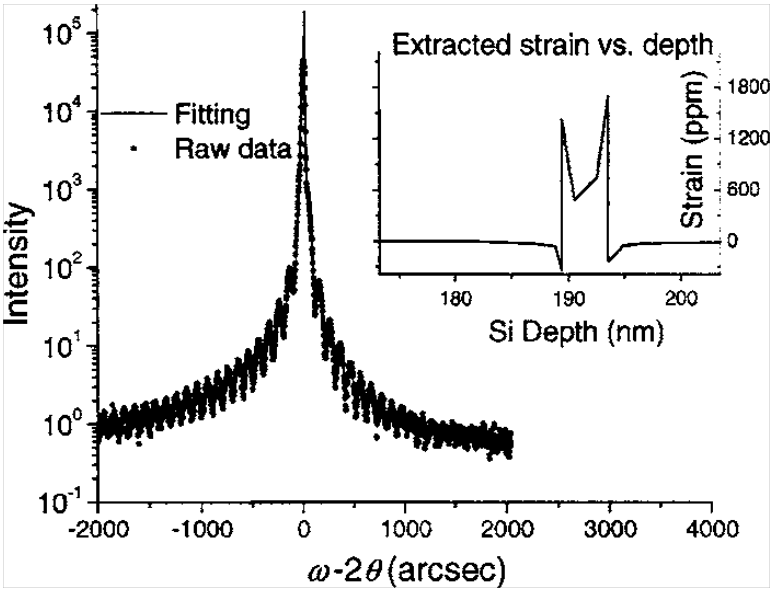

Fig. 39. Strain measured by X-ray diffraction in 190 nm Si/5 nm $Si_{0.8}Ge_{0.2}$/Si, from Shao *et al.* [30].

C. Conclusions

Strain in 50 nm thick surface compressively (in-plane) strained $Si_{0.8}Ge_{0.2}$ is stable under 2 MeV He ion irradiation to fluence around 3×10^{17} cm^{-2} due to repeated analysis. Electronic excitation due to high energy light ion irradiation is not sufficient to cause strain to change. Defect accumulation in the surface strained layer, however, does increase significantly with 2 MeV He ion irradiation.

Strain in 60 nm thick compressively (in-plane) strained $Si_{0.8}Ge_{0.2}$ layer buried beneath 50 nm Si is stable under 2 MeV He ion irradiation to fluence around 3×10^{17} cm^{-2} and 140 keV He ion irradiation to fluence 5×10^{16} cm^{-2}. Electronic excitation and nuclear collisions due to high and medium energy light ion irradiation are not sufficient at the reported fluences to cause strain to change. Defect accumulation in the buried strained $Si_{0.8}Ge_{0.2}$ layer is suppressed compared to surface strained $Si_{0.8}Ge_{0.2}$ layer.

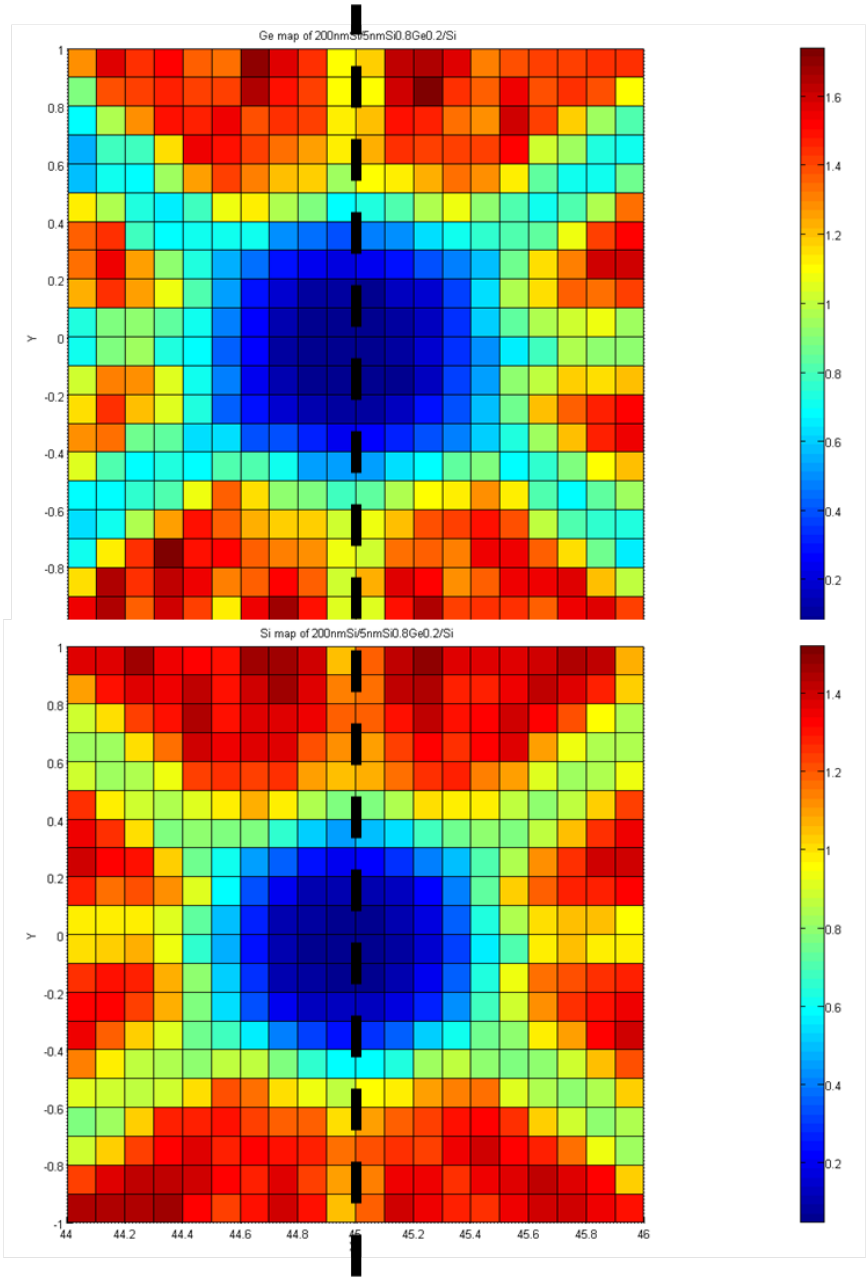

Fig. 40. Two-dimensional backscattering yield maps about the ⟨110⟩ axis of 190 nm Si/5 nm $Si_{0.8}Ge_{0.2}$/Si. Top is from surface Si layer and bottom is from Ge in buried $Si_{0.8}Ge_{0.2}$ layer. The difference in the position of the minimum yield in each map is less than the error associated with the measurement (0.05°).

For two-dimensional backscattering yield mapping of strained layer superlattices, composition of the layer as well as the alignment of the sample with the ion beam dictates asymmetry in the ⟨110⟩ axial channel. For a sample with a 50 nm thick $Si_{0.8}Ge_{0.2}$ strained surface layer where the alignment of the ion beam was performed with respect to Ge in the surface strained layer, the backscattering yield map is asymmetric about the ⟨110⟩ axis, with the channel appearing elliptical. Additionally, mapping the ⟨110⟩ axis of the unstrained, bulk Si buried underneath the strained layer gives an asymmetric axial channel. For a sample with a 50 nm thick Si unstrained surface layer where the alignment of the ion beam was performed with respect to the surface layer, the backscattering yield map is symmetric about the ⟨110⟩ axis, appearing circular in the low yield region. Backscattering yield maps of buried 60 nm thick $Si_{0.8}Ge_{0.2}$ appear highly asymmetrical, with one half of the channel appears semi-circular and the other half of the channel looks like a right triangle. The planes in these maps are also highly distorted. Though the layers have the same composition and similar thicknesses, mapping of the ⟨110⟩ axis of surface and buried strained $Si_{0.8}Ge_{0.2}$ layers gives different results. In both cases, the ion beam is sufficiently well-aligned with the sample to be in channeling mode, but the slight difference in alignment greatly effects the shape of the ⟨110⟩ channel as measured by backscattering yield mapping.

For a compressively (in-plane) strained $Si_{0.8}Ge_{0.2}$ layer, the first interface of the layer must be less than 190 nm below the surface to be analyzed with 2 MeV He by the method of backscattering yield mapping. In a 190 nm Si/5 nm $Si_{0.8}Ge_{0.2}$/Si sample, analysis by 2 MeV He indicates that there is no strain in the SiGe layer, which has been confirmed as strained previoulsy.

CHAPTER VIII

CONCLUSIONS OF STUDY OF ION IRRADIATION RESPONSE OF SILICON-GERMANIUM STRAINED LAYER SUPERLATTICES

A. Decreased Radiation Tolerance of Surface Strained SiGe Layer

This study confirms that, when subjected to ion irradiation, strained SiGe accumulates point defects more rapidly than bulk Si. Point defect accumulation saturated after a low fluence of 140 keV He ion irradiation in bulk Si, but increased linearly in strained SiGe from low to high fluence of 140 keV He ion irradiation.

B. Amorphization Model of Surface Strained SiGe Layer

Analysis of the amount of crystalline defects created by cluster ion irradiation revealed that greater crystalline damage is created by overlapping of multiple ion collision cascades in both surface strained SiGe layer and bulk Si. Strained SiGe and bulk Si do not differ in their amorphization models. An individual damage cascade forms a partially damaged, not amorphized, volume which must overlap with another partially damaged volume to form permanent damage, or amorphization, in both strained SiGe and bulk Si. Thus, decreased radiation tolerance of strained SiGe must be the result of the defect recombination process.

C. Strain Stability and Point Defect Accumulation of 140 keV and 2 MeV He Ion Irradiated Surface and Buried Strained SiGe Layers

Rutherford backscattering spectrometry in channeling mode with 2 MeV He ions proved to be destructive to surface strained SiGe layer, but not to a strained SiGe layer buried under a 50 nm Si layer. Radiation tolerance of strained SiGe is enhanced

when buried under an unstrained layer. Furthermore, irradiation of a buried strained layer with 140 keV He ions to fluences reported in Chapter V did not produce a significant increase in point defect concentration when compared with the unirradiated buried strained layer as measured by 2 MeV He multi-axial channeling RBS. Point defect accumulation does not effect the amount of strain as measured by multi-axial channeling Rutherford backscattering spectrometry with 2 MeV He ions in the surface strained layer. Relaxation of strain in the surface strained SiGe layer after high fluence 2 MeV He ion irradiation was not observed.

REFERENCES

[1] G. F. Knoll, *Radiation Detection and Measurement*, New York: John Wiley and Sons, Inc., 2000.

[2] M. Vos, C. Wu, I. V. Mitchell, T. E. Jackman, J.-M. Baribeau, and J. McCaffrey, "Selective amorphization of ion-bombarded sige strained-layer superlattices," *Applied Physics Letters*, vol. 58, pp. 951, 1991.

[3] D. J. Eaglesham, J. M. Poate, D. C. Jacobson, M. Cerullo, L. N. Pfeiffer, and K. West, "Fabrication of amorphous-crystalline superlattices in gesi-si and gaas-alas," *Applied Physics Letters*, vol. 58, no. 5, pp. 523–525, 1991.

[4] T. E. Haynes and O. W. Holland, "Damage accumulation during ion implantation of unstrained si[sub 1 - x]ge[sub x] alloy layers," *Applied Physics Letters*, vol. 61, no. 1, pp. 61–63, 1992.

[5] P. I. Gaiduk, J. Lundsgaard Hansen, A. Nylandsted Larsen, and E. A. Steinman, "Nanovoids in mbe-grown sige alloys implanted in situ with *ge*+ ions," *Phys. Rev. B*, vol. 67, no. 23, pp. 235310, Jun 2003.

[6] V. C. Venezia, D. J. Eaglesham, T. E. Haynes, Aditya Agarwal, D. C. Jacobson, H.-J. Gossmann, and F. H. Baumann, "Depth profiling of vacancy clusters in mev-implanted si using au labeling," *Applied Physics Letters*, vol. 73, no. 20, pp. 2980–2982, 1998.

[7] L. Esaki, "A bird's-eye view on the evolution of semiconductor superlattices and quantum wells," *IEEE Journal of Quantum Electronics*, vol. 22, pp. 1611–1624, 1986.

[8] G. Osbourn, "Strained-layer superlattices: A brief review," *Quantum Electronics, IEEE Journal of*, vol. 22, no. 9, pp. 1677–1681, Sep 1986.

[9] S. R. Sheng, M. Dion, S. P. McAlister, and N. L. Rowell, "Growth and characterization of si/sige strained-layer superlattices on bulk single-crystal sige and si substrates," *Journal of Crystal Growth*, vol. 253, no. 1-4, pp. 77 – 84, 2003.

[10] M.L. Lee, E.A. Fitzgerald, M.T. Bulsara, M.T. Currie, and A. Lochtefeld, "Strained si, sige, and ge channels for high-mobility metal-oxide- semiconductor field-effect transistors," *Journal of Applied Physics*, vol. 97, no. 1, pp. 011101–1–011101–27, 2005.

[11] A. T. Fiory, J. C. Bean, L. C. Feldman, and I. K. Robinson, "Commensurate and incommensurate structures in molecular beam epitaxially grown ge[sub x]si[sub 1 - x]films on si(100)," *Journal of Applied Physics*, vol. 56, no. 4, pp. 1227–1229, 1984.

[12] B. W. Dodson and J. Y. Tsao, "Relaxation of strained-layer semiconductor structures via plastic flow," *Applied Physics Letters*, vol. 51, no. 17, pp. 1325–1327, 1987.

[13] A. C. Churchill, D. J. Robbins, D. J. Wallis, N. Griffin, D. J. Paul, A. J. Pidduck, W. Y. Leong, and G. M. Williams, "Two-dimensional electron gas mobility as a function of virtual substrate quality in strained si/sige heterojunctions," *Papers from the Conference on Silicon Heterostructures: From Physics to Devices*, vol. 16, no. 3, pp. 1634–1638, 1998.

[14] W.K. Chu, J.W. Mayer, and M.-A. Nicolet, *Backscattering Spectrometry*, New York: Academic Press, 1978.

[15] L.C. Feldman and J.W. Mayer, *Fundamentals of Surface and Thin Film Analysis*, New York: North-Holland, 1986.

[16] J.R Tesmer and M. Nastasi, Eds., *Handbook of Modern Ion Beam Materials Analysis*, Pittsburgh, PA: MRS, 1995.

[17] J. Lindhard, "Influence of crystal lattice on motion of energetic charged particles," *Mat. Fys. Medd. Dan. Vid. Selsk.*, vol. 34, no. 14, 1965.

[18] M. L. Swanson, "The study of lattice defects by ion channeling," *Reports on Progress in Physics*, vol. 45, pp. 47, 1982.

[19] L. M. Howe, M. L. Swanson, and J. A. Davies, *Methods of Experimental Physics*, vol. 21, New York: Academic Press, 1983.

[20] T. L. Alford, L. C. Feldman, and J. W. Mayer, *Fundamentals of Nanoscale Film Analysis*, New York: Springer Science+Business Media, Inc., 2007.

[21] L. C. Feldman, J. Bevk, B. A. Davidson, H.-J. Gossmann, and J. P. Mannaerts, "Strain in ultrathin epitaxial films of ge/si(100) measured by ion scattering and channeling," *Phys. Rev. Lett.*, vol. 59, no. 6, pp. 664–667, Aug 1987.

[22] W. K. Chu, C. K. Pan, and C. A. Chang, "Superlattice interface and lattice strain measurement by ion channeling," *Phys. Rev. B*, vol. 28, no. 7, pp. 4033–4036, Oct 1983.

[23] D. Wijesundera, K. Ma, X. Wang, B. Liu, J.-R. Liu, and W.-K. Chu, "A geometric procedure for improved rutherford backscattering channeling analysis of materials," *Nuclear Instruments and Methods in Physics Research Section B: Beam Interactions with Materials and Atoms*, vol. 267, no. 11, pp. 1948 – 1951, 2009.

[24] M. Martin, P. E. Thompson, J. Carter, L. Zhu, M. Hollander, and L. Shao, "Damage creation in ion irradiated si1-xgex/si structures," *Nuclear Instruments and Methods in Physics Research Section B: Beam Interactions with Materials and Atoms*, vol. 266, no. 10, pp. 2483 – 2485, 2008.

[25] J. F. Gibbons, "Ion implantation in semiconductors — part ii: Damage production and annealing," *Proceedings of the IEEE*, vol. 60, no. 9, pp. 1062–1096, September 1972.

[26] J. R. Dennis and E. B. Hale, "Crystalline to amorphous transformation in ion-implanted silicon: A composite model," *Journal of Applied Physics*, vol. 49, no. 3, pp. 1119–1127, 1978.

[27] L. Shao, M. Nastasi, X. Wang, J. R. Liu, and W.-K. Chu, "A model for damage caused by cluster implantation: Non-linear effect due to damage overlap," *Nuclear Instruments and Methods in Physics Research Section B: Beam Interactions with Materials and Atoms*, vol. 242, no. 1-2, pp. 503 – 505, 2006, Ion Beam Modification of Materials - Proceedings of the 14th International Conference on Ion Beam Modification of Materials.

[28] P. Sigmund, G.P. Scheidler, and G. Roth, "Spatial distribution of defects in cascades," in *Proc. of the Int'l Conf. on Solid-State-Physics Research with Accelerators*, A.N. Goland, Ed. Brookhaven National Laboratory, 1968, p. 374, Technical Report BNL-50083.

[29] J. F. Ziegler, "Srim-2003," *Nuclear Instruments and Methods in Physics Research Section B: Beam Interactions with Materials and Atoms*, vol. 219-220, pp. 1027 – 1036, 2004, Proceedings of the Sixteenth International Conference on Ion Beam Analysis.

[30] L. Shao, Y. Q. Wang, J. G. Swadener, M. Nastasi, P. E. Thompson, and N. D. Theodore, "Cracking in hydrogen ion-implanted si/si[sub 0.8]ge[sub 0.2]/si heterostructures," *Applied Physics Letters*, vol. 92, no. 6, pp. 061904, 2008.

VITA

Michael Scott Martin began his pursuit of a Bachelor of Science in Nuclear Engineering at Texas A&M University in January 2003 and received that degree in December 2006. Due to his lack of interest in receiving a substantial income for many years, he enrolled in graduate school to pursue additional education in the Department of Nuclear Engineering at Texas A&M University under the advisement of Dr. Lin Shao and has no regrets. Michael can be reached at

Dept. of Nucl. Engr.
129 Zachry Mailstop 3133
College Station, TX 77843-3133

The typist for this thesis was Michael Martin.